

# Density functional theory of resonant inelastic x-ray scattering in the quasi-one-dimensional dimer iridate $\text{Ba}_5\text{AlIr}_2\text{O}_{11}$

D.A. Kukusta,<sup>1</sup> L.V. Bekenov,<sup>1</sup> and V.N. Antonov<sup>1,2</sup>

<sup>1</sup>*G. V. Kurdyumov Institute for Metal Physics of the N.A.S. of Ukraine,  
36 Academician Vernadsky Boulevard, UA-03142 Kyiv, Ukraine*

<sup>2</sup>*Max-Planck-Institute for Solid State Research, Heisenbergstrasse 1, 70569 Stuttgart, Germany  
(Dated: April 21, 2025)*

We have investigated the electronic structure of  $\text{Ba}_5\text{AlIr}_2\text{O}_{11}$  within the density functional theory using the generalized gradient approximation while considering strong Coulomb correlations in the framework of the fully relativistic spin-polarized Dirac linear muffin-tin orbital band-structure method. We have investigated the x-ray absorption spectra, x-ray magnetic circular dichroism, and resonant inelastic x-ray scattering spectra (RIXS) at the Ir  $K$ ,  $L_3$ ,  $M_3$ ,  $M_5$  and O  $K$  edges. The calculated results are in good agreement with experimental data. The RIXS spectrum of  $\text{Ba}_5\text{AlIr}_2\text{O}_{11}$  at the Ir  $L_3$  edge possesses sharp twelve features  $\leq 1.5$  eV corresponding to transitions within the Ir  $t_{2g}$  levels. The excitations located from 2 to 4 eV are due to  $t_{2g} \rightarrow e_g$  and  $\text{O}_{2p} \rightarrow t_{2g}$  transitions. The high energy peaks situated at 5–11 eV appear due to charge transfer transitions. The theory reproduces well the shape and polarization dependence of the oxygen O  $K$  RIXS spectrum. We have found that the dependence of the RIXS spectrum at the oxygen  $K$  edge on the incident photon energy and the momentum transfer vector  $\mathbf{Q}$  is much stronger than the corresponding dependence at the Ir  $L_3$  edge.

PACS numbers: 75.50.Cc, 71.20.Lp, 71.15.Rf

## I. INTRODUCTION

In recent years,  $5d$  transition-metal oxides attract wide scientific interest. Due to the extended nature of  $5d$  wave functions and wide energy bands these oxides were expected to be weakly correlated metals. However, surprisingly they often possess Mott-insulating states with unusual electronic and magnetic properties [1, 2]. In  $5d$  systems, due to the strong spin-orbit coupling (SOC) the  $t_{2g}$  orbitals split into a quartet ( $J_{\text{eff}} = 3/2$ ) and a doublet ( $J_{\text{eff}} = 1/2$ ) [3–5]. When incorporated with electron correlations, SOC can give rise to some fascinating phenomena, such as topological insulators [6–9], Mott insulators [1–3, 10, 11], Weyl semimetals [12–14], and quantum spin liquids [3, 15]. So far, most research has largely focused on  $\text{Ir}^{4+}$  iridium oxides with a  $t_{2g}^5$  configuration [1, 2, 10, 11, 16–23]. In these oxides, the quartet  $J_{\text{eff}} = 3/2$  is fully occupied, and the relatively narrow  $J_{\text{eff}} = 1/2$  doublet occupied by one electron can be split by moderate Hubbard  $U_{\text{eff}}$  with opening a small band gap called the relativistic Mott gap [1, 11, 24].

In  $5d^4$  iridium oxides, the  $\text{Ir}^{5+}$  ions realize completely filled  $J_{\text{eff}} = 3/2$  and empty  $J_{\text{eff}} = 1/2$  submanifolds. For a  $t_{2g}^4 e_g^0$  electron configuration the system is expected to be nonmagnetic in both the weakly and strongly correlated limits. In the weakly correlated picture, when SOC dominates over Hund's coupling,  $t_{2g}$  shells are split into a fully filled  $J_{\text{eff}} = 3/2$  shell and an empty  $J_{\text{eff}} = 1/2$  shell with a band gap between them, which leads to a nonmagnetic insulating ground state. In the strongly correlated picture, the first two Hund's rules require each  $d^4$  site to have total spin  $S = 1$  and total orbital  $L = 1$  moments. SOC yields a local  $J = 0$  state on every ion with a nonmagnetic ground state

[25, 26]. Although octahedrally coordinated  $\text{Re}^{3+}$ ,  $\text{Os}^{4+}$ , and  $\text{Ir}^{5+}$  systems with a  $5d^4$  electronic configuration have been studied since 1960s [27], they have been largely ignored in the literature. Recent theoretical and experimental studies suggest that novel magnetic states in iridates with pentavalent ions can emerge from the competition between the exchange interaction, noncubic crystal field, singlet-triplet splitting, and SOC [28–30].

Most studies of iridates have focused on two- or three-dimensional systems [30, 31]. Quasi-one-dimensional iridates have been investigated to a lesser extent, especially those with so called dimers, commonly found in transition-metal materials, and those in which the average number of electrons per transition metal is nonintegral. Dimerization in transition metal compounds is observed in many systems, e.g., in vanadium oxides [32, 33], titanates with the spinel structure [34],  $\alpha\text{-TiCl}_3$  [35],  $\alpha\text{-MoCl}_3$  [36],  $\text{Li}_2\text{RuO}_3$  [37], and  $\alpha\text{-RuCl}_3$  [38, 39]. The hyperhoneycomb iridate  $\beta\text{-Li}_2\text{IrO}_3$  in the high-pressure phase above 4 GPa is characterized by the formation of  $\text{Ir}_2$  dimers on zigzag chains. In the dimer phase the spin-orbital-entangled  $J_{\text{eff}} = \frac{1}{2}$  states break down, associated with the stabilization of the bonding state of neighboring  $d_{zx}$  orbitals [23, 24, 40]. A number of dimerized or cluster  $4d$  and  $5d$  compounds with intriguing properties have been synthesized recently [41–44].

Here we report the theoretical investigation of the electronic and magnetic structures of  $\text{Ba}_5\text{AlIr}_2\text{O}_{11}$ . The crystal structure of this compound consists of  $\text{MO}_6$  and  $\text{IrO}_6$  octahedra. The latter octahedra share a face and develop  $\text{Ir}_2\text{O}_9$  dimers, which spread along the  $b$  axis. Therefore, the compound would become geometrically frustrated in the presence of antiferromagnetic (AFM) interaction. Novel properties are expected from this struc-

tural arrangement in addition to those driven by SOC.  $\text{Ba}_5\text{AlIr}_2\text{O}_{11}$  features dimer chains of two inequivalent octahedra occupied by tetravalent  $\text{Ir}^{4+}$  ( $5d^5$ ) and pentavalent  $\text{Ir}^{5+}$  ( $5d^4$ ) ions, respectively.  $\text{Ba}_5\text{AlIr}_2\text{O}_{11}$  is a Mott insulator that undergoes a subtle structural phase transition near  $T_S = 210$  K and a transition to magnetic order at  $T_M = 4.5$  K. The ferrimagnetic (FiM) state below  $T_M$  is highly anisotropic and resilient to a strong magnetic field (up to 14 T) but is susceptible to even modest hydrostatic pressure [30]. There are anomalies in the electrical resistivity, dielectric constant, specific heat, and lattice parameters observed at  $T_S = 210$  K. The experimental data indicate that the degree of charge order between  $\text{Ir}^{4+}$  and  $\text{Ir}^{5+}$  ions is increased below  $T_S$ .

In this work we consider the RIXS properties of  $\text{Ba}_5\text{AlIr}_2\text{O}_{11}$ . Since the first publication by Kao *et al.* on NiO [45], the RIXS method has shown remarkable progress as a spectroscopic technique to record the momentum and energy dependence of inelastically scattered photons in complex materials. RIXS rapidly became the forefront of experimental photon science [46, 47]. It combines spectroscopy and inelastic scattering to probe the electronic structure of materials. This method is an element- and orbital- selective X-ray spectroscopy technique based on a two-step, two-photon resonant process. It combines X-ray emission spectroscopy (XES) with X-ray absorption spectroscopy (XAS) by measuring the coherent X-ray emission at an incident X-ray photon energy within the near edge X-ray absorption spectrum. In the first step (X-ray absorption), an electron of the absorbing atom is resonantly excited from a core level to an empty state. The resulting intermediate state carries a core hole with a very small lifetime. In the second step (X-ray emission), the system radiatively decays into a final state in which the core hole is filled by another electron accompanied by photon-out emission. The polarization of the incoming and outgoing light and the resonant energy are involved in the RIXS process, making RIXS a simultaneous spectroscopy and scattering technique. RIXS has a number of unique features in comparison with other spectroscopic techniques. It covers a large scattering phase space and requires only small sample volumes. It is also bulk sensitive, polarization dependent, as well as element and orbital specific [46]. A detail comparison with other spectroscopic technics can be found in the recent review article [47]. The spectral broadening owing to a short core hole lifetime can be reduced to produce RIXS spectra with high resolution. It permits direct measurements of phonons, plasmons, single-magnon, and orbitons as well as other many-body excitations in strongly correlated systems, such as cuprates, nickelates, osmates, ruthenates, and iridates, with complex low-energy physics and exotic phenomena in the energy and momentum space.

There has been great progress in the RIXS experiments over the past decade. Most calculations of RIXS spectra of various materials have been performed using the atomic multiplet approach with some adjustable param-

eters while the number of first-principle calculations of RIXS spectra is extremely limited. In this paper we report a theoretical first-principle study of the RIXS spectra of  $\text{Ba}_5\text{AlIr}_2\text{O}_{11}$ . The RIXS spectra at the Ir  $L_3$  edge in  $\text{Ba}_5\text{AlIr}_2\text{O}_{11}$  were measured by Wang *et al.* [48] and Katukuri *et al.* [49]. The former authors measure the RIXS spectrum for interband transitions inside  $t_{2g}$  bands up to 1.2 eV. The latter authors present the RIXS spectrum for a larger energy interval of 0-8 eV. Both measurements show similar spectra at 0-1.2 eV. Wang *et al.* [48] used a two-site cluster model with some adjustable parameters to simulate the measured Ir  $L_3$  RIXS spectrum. Katukuri *et al.* [49] to calculate the RIXS exciton energies also used a quantum chemistry cluster model, which contains one  $\text{Ir}_2\text{O}_9$  dimer unit, two neighboring  $\text{AlO}_4$  tetrahedra and 15 surrounding  $\text{Ba}^{2+}$  ions. This cluster was embedded in a set of point charges that reproduce the electrostatic effects of the solid state environment. The RIXS spectra at the O  $K$  edge in  $\text{Ba}_5\text{AlIr}_2\text{O}_{11}$  were measured by Katukuri *et al.* [49] for two different  $\pi$  and  $\sigma$  polarizations up to 10 eV. They also presented the polarization dependence of the XAS spectra at the oxygen  $K$  edge.

We carry out here a detailed study of the electronic structure, XAS, XMCD (x-ray magnetic circular dichroism), and RIXS spectra of  $\text{Ba}_5\text{AlIr}_2\text{O}_{11}$  in terms of the density functional theory (DFT). Our study sheds light on the role of band structure effects and transition metal  $5d$  – oxygen  $2p$  hybridization in the spectral properties of  $5d$  oxides. The energy band structure, the XAS, XMCD, and RIXS spectra of  $\text{Ba}_5\text{AlIr}_2\text{O}_{11}$  are investigated in the *ab initio* approach using the fully relativistic spin-polarized Dirac linear muffin-tin orbital (LMTO) band structure method. We use both the generalized gradient approximation (GGA) and the GGA+ $U$  approach to assess the sensitivity of the RIXS results to different treatment of correlated electrons.

The article is organized as follows. The crystal structure of  $\text{Ba}_5\text{AlIr}_2\text{O}_{11}$  and computational details are presented in Sec. II. Section III presents the electronic and magnetic structures of  $\text{Ba}_5\text{AlIr}_2\text{O}_{11}$ . In Sec. IV, the theoretical investigations of the XAS, XMCD, and RIXS spectra of  $\text{Ba}_5\text{AlIr}_2\text{O}_{11}$  at the Ir  $K$ ,  $L_3$ ,  $M_3$ , and  $M_5$  edges are presented, the theoretical results are compared with the experimental measurements. In Sec. V we present the theoretical investigations of the XAS and RIXS spectra at the O  $K$  edge. Finally, the results are summarized in Sec. VI.

## II. COMPUTATIONAL DETAILS

### A. X-ray magnetic circular dichroism.

Magneto-optical (MO) effects refer to various changes in the polarization state of light upon interaction with materials possessing a net magnetic moment, including rotation of the plane of linearly polarized light (Fara-

day, Kerr rotation), and the complementary differential absorption of left and right circularly polarized light (circular dichroism). In the near visible spectral range these effects result from excitation of electrons in the conduction band. Near x-ray absorption edges, or resonances, magneto-optical effects can be enhanced by transitions from well-defined atomic core levels to transition symmetry selected valence states [50].

Within the one-particle approximation, the absorption coefficient  $\mu_j^\lambda(\omega)$  for incident x-ray polarization  $\lambda$  and photon energy  $\hbar\omega$  can be determined as the probability of electronic transitions from initial core states with the total angular momentum  $j$  to final unoccupied Bloch states

$$\mu_j^\lambda(\omega) = \sum_{m_j} \sum_{n\mathbf{k}} |\langle \Psi_{n\mathbf{k}} | \Pi_\lambda | \Psi_{jm_j} \rangle|^2 \delta(E_{n\mathbf{k}} - E_{jm_j} - \hbar\omega) \times \theta(E_{n\mathbf{k}} - E_F), \quad (1)$$

where  $\Psi_{jm_j}$  and  $E_{jm_j}$  are the wave function and the energy of a core state with the projection of the total angular momentum  $m_j$ ;  $\Psi_{n\mathbf{k}}$  and  $E_{n\mathbf{k}}$  are the wave function and the energy of a valence state in the  $n$ -th band with the wave vector  $\mathbf{k}$ ;  $E_F$  is the Fermi energy.

$\Pi_\lambda$  is the electron-photon interaction operator in the dipole approximation

$$\Pi_\lambda = -e\boldsymbol{\alpha}\mathbf{a}_\lambda, \quad (2)$$

where  $\boldsymbol{\alpha}$  are the Dirac matrices and  $\mathbf{a}_\lambda$  is the  $\lambda$  polarization unit vector of the photon vector potential, with  $a_\pm = 1/\sqrt{2}(1, \pm i, 0)$ ,  $a_\parallel = (0, 0, 1)$ . Here,  $+$  and  $-$  denote, respectively, left and right circular photon polarizations with respect to the magnetization direction in the solid. Then, x-ray magnetic circular and linear dichroisms are given by  $\mu_+ - \mu_-$  and  $\mu_\parallel - (\mu_+ + \mu_-)/2$ , respectively. More detailed expressions of the matrix elements in the electric dipole approximation may be found in Refs. [50–52]. The matrix elements due to magnetic dipole and electric quadrupole corrections are presented in Ref. [52].

## B. RIXS

In the direct RIXS process [46] the incoming photon with energy  $\hbar\omega_{\mathbf{k}}$ , momentum  $\hbar\mathbf{k}$ , and polarization  $\boldsymbol{\epsilon}$  excites the solid from the ground state  $|g\rangle$  with energy  $E_g$  to the intermediate state  $|I\rangle$  with energy  $E_I$ . During relaxation an outgoing photon with energy  $\hbar\omega_{\mathbf{k}'}$ , momentum  $\hbar\mathbf{k}'$  and polarization  $\boldsymbol{\epsilon}'$  is emitted, and the solid is in state  $|f\rangle$  with energy  $E_f$ . As a result, an excitation with energy  $\hbar\omega = \hbar\omega_{\mathbf{k}} - \hbar\omega_{\mathbf{k}'}$  and momentum  $\hbar\mathbf{q} = \hbar\mathbf{k} - \hbar\mathbf{k}'$  is created. Our implementation of the code for the calculation of the RIXS intensity uses Dirac four-component basis functions [53] in the perturbative approach [54]. RIXS is the second-order process, and its intensity is given by

TABLE I: The Wyckoff symbols (WS) and atomic positions ( $x, y, z$ ) for  $\text{Ba}_5\text{AlIr}_2\text{O}_{11}$  with the  $Pnma$  structure at room temperature (the lattice constants  $a = 18.8360$ ,  $b = 5.7887$ , and  $c = 11.103$  Å) [56].

WS	Atom	$x$	$y$	$z$
4c	Ba <sub>1</sub>	0.1380	0.25	0.1920
4c	Ba <sub>2</sub>	0.9312	0.25	0.0277
4c	Ba <sub>3</sub>	0.4728	0.25	0.1048
4c	Ba <sub>4</sub>	0.1747	0.25	0.5485
4c	Ba <sub>5</sub>	0.7510	0.25	0.6230
4c	Ir <sub>1</sub>	0.5666	0.25	0.7035
4c	Ir <sub>2</sub>	0.9319	0.25	0.7062
4c	Al	0.8110	0.25	0.2586
4c	O <sub>1</sub>	0.2540	0.25	0.365
4c	O <sub>2</sub>	0.5280	0.25	0.883
4c	O <sub>3</sub>	0.3490	0.25	0.692
4c	O <sub>4</sub>	0.2710	0.25	0.101
4c	O <sub>5</sub>	0.5950	0.25	0.538
8d	O <sub>6</sub>	0.4850	0.021	0.684
8d	O <sub>7</sub>	0.3980	0.482	0.901
8d	O <sub>8</sub>	0.3650	0.494	0.254

$$I(\omega, \mathbf{k}, \mathbf{k}', \boldsymbol{\epsilon}, \boldsymbol{\epsilon}') \propto \sum_{\mathbf{f}} \left| \sum_{\mathbf{I}} \frac{\langle \mathbf{f} | \hat{H}'_{\mathbf{k}'\boldsymbol{\epsilon}'} | \mathbf{I} \rangle \langle \mathbf{I} | \hat{H}'_{\mathbf{k}\boldsymbol{\epsilon}} | \mathbf{g} \rangle}{E_g - E_I} \right|^2 \times \delta(E_f - E_g - \hbar\omega), \quad (3)$$

where the RIXS perturbation operator in the dipole approximation is given by the lattice sum  $\hat{H}'_{\mathbf{k}\boldsymbol{\epsilon}} = \sum_{\mathbf{R}} \hat{\boldsymbol{\alpha}} \exp(-i\mathbf{k}\mathbf{R})$ , where  $\hat{\boldsymbol{\alpha}}$  are the Dirac matrices. The sum over the intermediate states  $|\mathbf{I}\rangle$  includes the contributions from different spin-split core states at the given absorption edge. The matrix elements of the RIXS process in the frame of the fully relativistic Dirac LMTO method were presented in Ref. [55].

## C. Crystal structure.

Figure 1 shows the crystal structure of  $\text{Ba}_5\text{AlIr}_2\text{O}_{11}$ . It has the orthorhombic structure with space group  $Pnma$  (No. 62). The lattice parameters and Wyckoff positions are presented at Table I. The structure consists of  $\text{IrO}_6$  octahedra sharing a face along the crystallographic  $b$  axis, and develop so called  $\text{Ir}_2\text{O}_9$  dimers. Each dimer consists of two inequivalent octahedral  $\text{Ir}_1$  and  $\text{Ir}_2$  sites ( $\text{Ir}_2$  occupies octahedra, which share their corners with  $\text{AlO}_4$  tetrahedra;  $\text{Ir}_1$  is in the center of the remaining octahedra) occupied by pentavalent  $\text{Ir}^{5+}$  ( $5d^4$ ) and tetravalent  $\text{Ir}^{4+}$  ( $5d^5$ ) ions, respectively. These dimers are corner connected through  $\text{AlO}_4$  tetrahedra, forming dimer chains along the  $b$  axis, but the dimer chains are not connected along the  $a$  and  $c$  axes (Fig. 1).

$\text{Ba}_5\text{AlIr}_2\text{O}_{11}$  contains four formula units and hence four structural Ir dimers in the unit cell. The oxygen

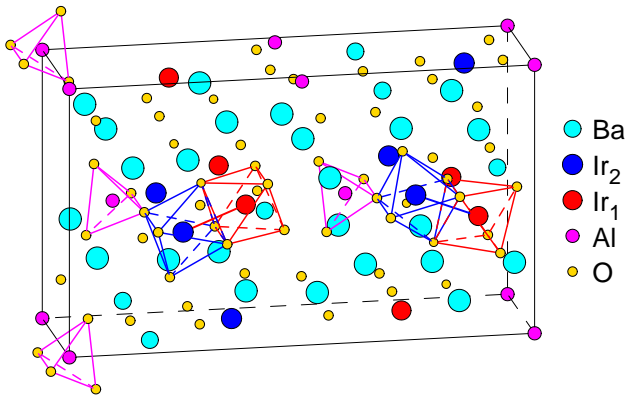


FIG. 1: (Color online) The schematic representation of the simple orthogonal  $Pnma$  (group number 62)  $Ba_5AlIr_2O_{11}$  crystal structure [56].

atoms surrounding the Ir sites provide an octahedral environment. The  $Ir_1-O_5$ ,  $Ir_1-O_8$ ,  $Ir_1-O_6$ , and  $Ir_1-O_2$  interatomic distances are equal to 1.9138, 2.0196, 2.0412, and 2.1215 Å, respectively. The corresponding distances for the  $Ir_2$  ion  $Ir_2-O_7$ ,  $Ir_2-O_3$ ,  $Ir_2-O_6$ , and  $Ir_2-O_2$  are equal to 1.9047, 1.9276, 2.0600, and 2.0634 Å respectively. The Al sites are provided by an oxygen tetrahedral environment. The Al-O interatomic distances are equal to 1.7314, 1.7424, and 1.7462 Å for Al- $O_4$ , Al- $O_1$ , Al- $O_8$ , respectively. The  $Ir_1-Ir_2$  intersite distance is equal to 2.72812 Å.

$Ba_5AlIr_2O_{11}$  undergoes a subtle structural phase transition near  $T_S = 210$  K and a magnetic order transition at  $T_M = 4.5$  K. By reducing the temperature from 300 to 100 K the  $a$ ,  $b$ , and  $c$  lattice constants are reduced approximately by 0.12, 0.22, and 0.25%, respectively. The volume of the unit cell is reduced from 1210.62 to 1194.84 Å<sup>3</sup>, the interatomic  $Ir_1-Ir_2$  distance is also reduced by approximately 0.01 Å. All results indicate that the phase transition at  $T_S$  signals an enhanced degree of charge order among the  $Ir^{4+}$  and  $Ir^{5+}$  ions [30, 56].

#### D. Calculation details

The details of the computational method are described in our previous papers [55, 58–60] and here we only mention several aspects. The band structure calculations were performed using the fully relativistic LMTO method [50, 61]. This implementation of the LMTO method uses four-component basis functions constructed by solving the Dirac equation inside an atomic sphere [53]. The exchange-correlation functional of the GGA-type was used in the version of Perdew *et al.* [62]. The Brillouin zone integration was performed using the improved tetrahedron method [63]. The basis consisted of Ir, Ba, and Al  $s$ ,  $p$ ,  $d$ , and  $f$ ; and O  $s$ ,  $p$ , and  $d$  LMTO's.

To consider the electron-electron correlation effects, we used the relativistic generalization of the rotationally in-

variant version of the LSDA+ $U$  method [64] which considers that, in the presence of SOC, the occupation matrix of localized electrons becomes nondiagonal in spin indexes. Hubbard  $U$  was considered as an external parameter and varied from 0.65 to 3.65 eV. We used in our calculations the value of exchange Hund's coupling  $J_H = 0.65$  eV obtained from constrained LSDA calculations [65, 66]. Thus, the parameter  $U_{\text{eff}} = U - J_H$ , which roughly determines the splitting between the lower and upper Hubbard bands, varied between 0 and 3.0 eV. We adjusted the value of  $U$  to achieve the best agreement with the experiment.

In the RIXS process, an electron is promoted from a core level to an intermediate state, leaving a core hole. As a result, the electronic structure of this state is different from that of the ground state. To reproduce the experimental spectrum, the self-consistent calculations should be carried out including a core hole. Usually, the core-hole effect has no impact on the shape of XAS at the  $L_{2,3}$  edges of  $5d$  systems and just a minor effect on the XMCD spectra at these edges [50]. However, the core hole has a strong effect on the RIXS spectra in transition metal compounds [55, 67]; therefore, we consider it.

The XAS, XMCD, and RIXS spectra were calculated taking into account the exchange splitting of core levels. The finite lifetime of a core hole was accounted for by folding the spectra with a Lorentzian. The widths of core levels  $\Gamma$  for Os and O were taken from Ref. [57]. The finite experimental resolution of the spectrometer was accounted for by a Gaussian of 0.6 eV (the  $s$  coefficient of the Gaussian function).

Note that in our electronic structure calculations we rely on the experimentally measured atomic positions and lattice constants because they are well established for this material and are probably still more accurate than those obtained from DFT.

### III. ELECTRONIC AND MAGNETIC STRUCTURES

The electrical resistivity  $\rho$  in  $Ba_5AlIr_2O_{11}$  increases by nearly nine orders of magnitude when temperature is lowered from 750 K ( $10^2 \Omega\text{cm}$ ) to 80 K ( $10^{11} \Omega\text{cm}$ ).  $Ba_5AlIr_2O_{11}$  is a Mott insulator that undergoes a subtle structural phase transition near  $T_S = 210$  K and a magnetic order transition at  $T_M = 4.5$  K.  $\rho$  exhibits a distinct slope change near  $T_S = 210$  K and follows an activation law reasonably well (better than power laws) in a temperature range of 200–750 K, which yields the dielectric nature of  $Ba_5AlIr_2O_{11}$  with an activation energy gap  $\Delta_a \sim 0.57$  eV [30]. The more rapid increase in  $\rho$  below  $T_S$  indicates a charge-order transition which is accompanied by increasing of the electronic states localization. The dielectric constant  $\epsilon(T)$  and specific heat  $C(T)$  are also consistent with a bulk transition to long-range order at  $T_S$  [30].

We performed GGA, GGA+SO, and GGA+SO+ $U$

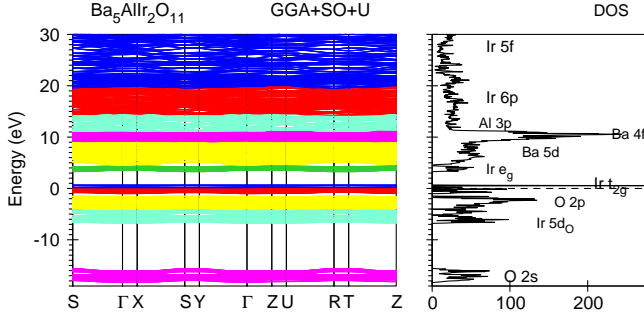


FIG. 2: (Color online) The energy band structure of  $\text{Ba}_5\text{AlIr}_2\text{O}_{11}$  calculated in the GGA+SO+ $U$  ( $U_{\text{eff}} = 0.6$  eV) approach.

calculations of the electronic and magnetic structures of  $\text{Ba}_5\text{AlIr}_2\text{O}_{11}$  for the experimental crystal structure [56]. Our GGA and GGA+SO band structure calculations produce a metallic solution for  $\text{Ba}_5\text{AlIr}_2\text{O}_{11}$  in contradiction to experiment. To produce the correct dielectric ground state, one has to take into account strong Coulomb correlations in  $\text{Ba}_5\text{AlIr}_2\text{O}_{11}$ . We found that the value of Hubbard  $U_{\text{eff}} = 0.6$  eV applied for the Ir sites produces the best agreement between the calculated and experimentally measured RIXS spectra at the Ir  $L_3$  edge in  $\text{Ba}_5\text{AlIr}_2\text{O}_{11}$ . The GGA+SO+ $U$  approach shifts the occupied  $t_{2g}$  bands downward and upward, respectively, by  $U_{\text{eff}}/2$  producing an energy gap of 0.126 eV for  $U_{\text{eff}} = 0.6$  eV. The energy gap is increased with increasing Hubbard  $U$ .

Figures 2 and 3 present the energy band structure and partial density of states (DOS) in  $\text{Ba}_5\text{AlIr}_2\text{O}_{11}$  calculated in the GGA+SO+ $U$  approach with  $U_{\text{eff}} = 0.6$  eV. The occupied  $t_{2g}$  states, the low energy band (LEB), are situated in the energy interval from  $-1$  eV to  $E_F$ . The empty  $t_{2g}$  states [the upper energy band (UEB)] consist of three narrow single peaks divided by energy gaps and occupy the energy range from 0.126 to 0.6 eV. The  $e_g$ -type states of Ir are distributed far above the Fermi level from 3.3 to 4.3 eV. The oxygen  $2s$  states lay at the bottom of the valence band and occupy the energy interval from  $-18.4$  to  $-15.6$  eV. The oxygen  $2p$  states occupy the energy interval from  $-4.0$  to  $-1.5$  eV and separate from Ir  $t_{2g}$  bands by an energy gap of 0.6 eV. It is interesting to note the existence of a strong and quite narrow O  $2p$  peak of 0.1 eV at the top of the oxygen  $2p$  band between  $-1.7$  and  $-1.5$  eV separated by the rest of the  $2p$  band by a small energy gap. The oxygen  $2p$  states are strongly hybridized with the Ir  $t_{2g}$  LEB and Ir  $t_{2g}$  UEB just below and above the Fermi level. The empty oxygen  $2p$  states are also strongly hybridized with Ir  $e_g$  states from 3.3 to 4.3 eV [Fig. 3(b)]. There is a significant amount of Ir  $5d$  DOS located at the bottom of oxygen  $2p$  states from  $-6.8$  to  $-4.1$  eV below the Fermi energy. The excessive charge is provided by the tails of oxygen  $2p$  states inside the Ir atomic spheres. These so called Ir

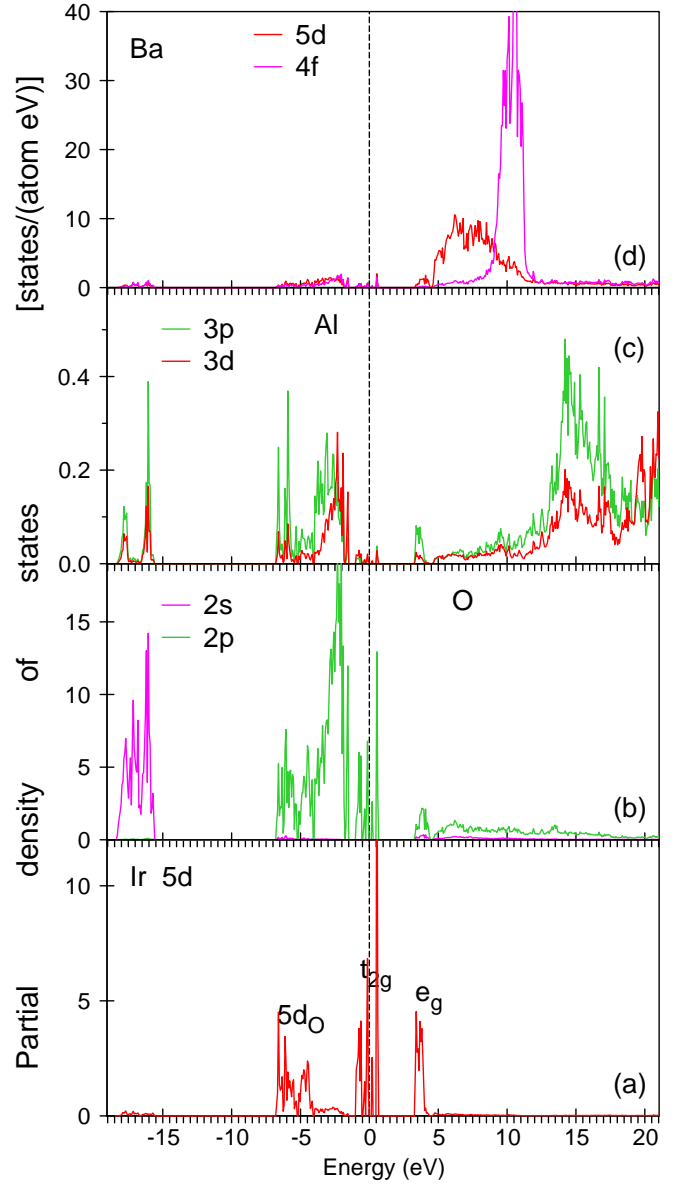


FIG. 3: (Color online) The partial density of states (DOS) for  $\text{Ba}_5\text{AlIr}_2\text{O}_{11}$  calculated in the GGA+SO+ $U$  ( $U_{\text{eff}} = 0.6$  eV) approach.

$5d_O$  states play an essential role in the RIXS spectrum at the Ir  $L_3$  edge (see Sec. IV). The Ba  $5d$  states occupy the energy region from 4.4 to 11.3 eV above the energy Fermi. A narrow and intensive DOS peak of Ba  $4f$  states are located just above the Ba  $5d$  states from 9.2 to 11.1 eV. The Al  $3p$  states lay between Ba  $4f$  and Ir  $6p$  states. The latter ones occupy the energy interval from 14.4 to 19.7 eV. Above this energy Ir  $5f$  states are situated.

Katukuri *et al.* [49] showed that formation of molecular orbitals is possible in  $\text{Ba}_5\text{AlIr}_2\text{O}_{11}$  when the Ir<sub>1</sub>-Ir<sub>2</sub> intersite distance is below 2.65 Å. In that case, a strongly hybridized  $a_{1g}$  type of orbitals is formed and the two irons in the Ir<sub>2</sub>O<sub>9</sub> dimer unit (Ir<sup>4+</sup> and Ir<sup>5+</sup>) preserve their

local  $J_{\text{eff}}$  character close to  $1/2$  and  $0$ , respectively. At room temperature the  $\text{Ir}_1\text{-Ir}_2$  intersite distance is equal to  $2.728 \text{ \AA}$  ( $\sim 2.72 \text{ \AA}$  below  $4 \text{ K}$ ). It is still too large for the formation of molecular orbitals in  $\text{Ba}_5\text{AlIr}_2\text{O}_{11}$ . The molecular orbitals can be created by an external or chemical pressure.

The average  $\text{Ir}_1\text{-O}$  bond distance  $d_{\text{Ir}_1\text{-O}}$  equals to  $2.024 \text{ \AA}$ , while the average  $\text{Ir}_2\text{-O}$  bond distance is  $1.989 \text{ \AA}$  at room temperature.  $d_{\text{Ir}_1\text{-O}} > d_{\text{Ir}_2\text{-O}}$  due to different oxidation states of the two Ir sites.  $d_{\text{Ir}_1\text{-O}}$  is longer most likely due to the relatively large ionic radius  $r$  of  $\text{Ir}^{4+}$  ( $r = 0.625$  and  $0.570 \text{ \AA}$  for  $\text{Ir}^{4+}$  and  $\text{Ir}^{5+}$ , respectively). Therefore, there is a tendency to charge ordering in  $\text{Ba}_5\text{AlIr}_2\text{O}_{11}$ . The charge ordering is supported by the structural transition and anomalies in  $\rho(T)$  and  $C(T)$  at  $T_S$  [30]. However, the charge disproportionation of  $\sim 0.3$  electron is not complete. Similar disproportionation was observed by Terzis *et al.* [30]. A purely ionic model with strong SOC, which would support  $J_{\text{eff}} = \frac{1}{2}$  in  $\text{Ir}_2^{4+}$  ( $5d^5$ ) and  $J_{\text{eff}} = 0$  in  $\text{Ir}_1^{5+}$  ( $5d^4$ ), is not entirely applicable in  $\text{Ba}_5\text{AlIr}_2\text{O}_{11}$ . Our GGA+SO+ $U$  calculations produce the ionicity equal to  $+4.3$  and  $+4.7$  for the  $\text{Ir}_1$  and  $\text{Ir}_2$  ions, respectively. We should mention, however, that usually the DFT approach overestimates the effect of hybridization between electronic states in crystals [50]. Therefore, one would expect the situation just in between the pure ionic and DFT pictures in  $\text{Ba}_5\text{AlIr}_2\text{O}_{11}$ .

Our calculations give a FiM solution for  $\text{Ba}_5\text{AlIr}_2\text{O}_{11}$ . The theoretically calculated spin magnetic moments are equal to  $-0.1293$  and  $0.4322 \mu_B$  for  $\text{Ir}_1$  and  $\text{Ir}_2$ , respectively (Table II). The orbital magnetic moment for  $\text{Ir}_1$ , which is supposed to be in  $5d^{4+}$  state, is equal to  $M_l^{\text{Ir}_1} = -0.2511 \mu_B$ . For the  $\text{Ir}_2^{+5}$  ion the orbital moment is small but does not vanish  $M_l^{\text{Ir}_2} = 0.0229 \mu_B$ . We can conclude that in the DFT approach there is no pure  $\text{Ir}^{4+}$  or  $\text{Ir}^{5+}$  states in  $\text{Ba}_5\text{AlIr}_2\text{O}_{11}$ . For example, the orbital magnetic moment in the  $J_{\text{eff}} = \frac{1}{2}$  Mott isolator  $\text{Sr}_2\text{IrO}_4$  at the  $\text{Ir}^{4+}$  site is  $M_l = 0.4447 \mu_B$  [68] which is almost two times larger than the corresponding orbital magnetic moment at the  $\text{Ir}_1$  site in  $\text{Ba}_5\text{AlIr}_2\text{O}_{11}$ .

The spin and orbital magnetic moments at the Al site are relatively small (both are equal to  $-0.0004 \mu_B$ ). The largest oxygen spin and orbital magnetic moments are found at the  $\text{O}_3$  and  $\text{O}_5$  sites (Table II). The Ba  $5d$  and  $4f$  states are almost completely empty in  $\text{Ba}_5\text{AlIr}_2\text{O}_{11}$  and the spin and orbital magnetic moments at the Ba sites are quite small.

#### IV. XAS, XMCD, AND RIXS SPECTRA

##### A. XAS and XMCD spectra at the Ir $L_{2,3}$ edges

Figure 4 presents the XAS (the upper panel) and XMCD spectra (the lower panel) at the Ir  $L_{2,3}$  edges for  $\text{Ba}_5\text{AlIr}_2\text{O}_{11}$  calculated in the GGA+SO+ $U$  ( $U_{\text{eff}} = 0.6 \text{ eV}$ ) approach for  $\text{Ir}_1$  (the full blue curves) and  $\text{Ir}_2$

TABLE II: The theoretical spin  $M_s$ , orbital  $M_l$ , and total  $M_{\text{tot}}$  magnetic moments ( $\mu_B$ ) in  $\text{Ba}_5\text{AlIr}_2\text{O}_{11}$  calculated in the GGA+SO+ $U$  approach ( $U_{\text{eff}} = 0.6 \text{ eV}$ ).

atom	$M_s$	$M_l$	$M_{\text{tot}}$
Ba <sub>1</sub>	0.0071	-0.0026	0.0045
Ba <sub>2</sub>	0.0069	0.0061	0.0130
Ba <sub>3</sub>	0.0076	-0.0007	0.0068
Ba <sub>4</sub>	0.0001	-0.0030	-0.0029
Ba <sub>5</sub>	0.0085	0.0032	0.0117
Ir <sub>1</sub>	-0.1293	-0.2511	-0.3804
Ir <sub>2</sub>	0.4322	0.0229	0.4551
Al	-0.0004	-0.0004	-0.0008
O <sub>1</sub>	-0.0028	0.0003	-0.0025
O <sub>2</sub>	0.0243	-0.0017	0.0226
O <sub>3</sub>	0.1443	-0.0113	0.1330
O <sub>4</sub>	0.0027	0.0005	0.0032
O <sub>5</sub>	-0.0382	-0.0668	-0.1050
O <sub>6</sub>	0.0193	0.0033	0.0226
O <sub>7</sub>	0.0362	0.0097	0.0459
O <sub>8</sub>	-0.0072	0.0029	-0.0043

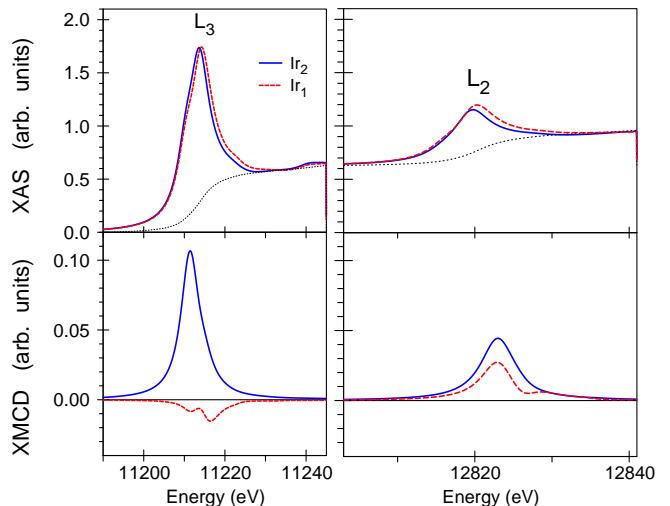


FIG. 4: (Color online) The theoretically calculated x-ray absorption (the upper panels) and XMCD spectra (the lower panels) at the Ir  $L_{2,3}$  edges in  $\text{Ba}_5\text{AlIr}_2\text{O}_{11}$  in the GGA+SO+ $U$  approach ( $U_{\text{eff}} = 0.6 \text{ eV}$ ). The dotted black curves in the upper panels show the background scattering intensity.

(the dashed red curves) sites. The isotropic XAS spectra are dominated by empty  $e_g$  states with a smaller contribution from empty  $t_{2g}$  orbitals at lower energy. The XMCD spectra, however, mainly come from the  $t_{2g}$  orbitals. This results in a shift between the maxima of the XAS and XMCD spectra.

Due to the importance of SOC effects in iridates, it is natural to quantify the strength of the SO interaction in these compounds. XAS provides one of the methods for this. Van der Laan and Thole showed that the so-called



branching ratio  $BR = I_{L_3}/I_{L_2}$  ( $I_{L_{2,3}}$  is the integrated intensity of isotropic XAS at the  $L_{2,3}$  edges) is an important quantity associated with SOI [69]. The BR is directly related to the ground-state expectation value of the angular part of the spin-orbit coupling  $\langle \mathbf{L} \cdot \mathbf{S} \rangle$  through  $BR = (2+r)/(1-r)$ , where  $r = \langle \mathbf{L} \cdot \mathbf{S} \rangle / n_h$  and  $n_h$  is the number of holes in  $5d$  states [69]. As a result, XAS provides a direct probe of SOI, which is complementary to other techniques such as the magnetic susceptibility, electron paramagnetic resonance, and Mössbauer spectroscopy (which probe SOC through the value of the Lande  $g$ -factor). In the limit of negligible SOC effects, the statistical branching ratio  $BR = 2$ , and the  $L_3$  white line is twice the size of the  $L_2$  feature [69]. The theoretically calculated BR in  $\text{Ba}_5\text{AlIr}_2\text{O}_{11}$  is 4.09 and 3.70 for the  $\text{Ir}_2$  and  $\text{Ir}_1$  sites, respectively, for the GGA+SO+ $U$  ( $U_{\text{eff}} = 0.6$  eV) approach. They differ significantly from the statistical  $BR = 2$  in the absence of orbital magnetization in  $5d$  states. A strong deviation from 2 indicates a strong coupling between the local orbital and spin moments.

There is a relatively large XMCD signal at the  $L_3$  edge for the  $\text{Ir}_1$  site. However, for the  $\text{Ir}_2$  site the dichroism is much smaller due to the smallness of the orbital magnetic moment at that site (see Table II).

### B. RIXS spectra at the Ir $L_3$ edge

The Ir  $L_{2,3}$  RIXS spectra occur from a local excitation between filled and empty  $5d$  states. More precisely, the incoming photon excites a  $2p_{1/2}$  core electron ( $L_2$  spectrum) or a  $2p_{3/2}$  one ( $L_3$  spectrum) into an empty  $5d$  state, which is followed by the de-excitation from the occupied  $5d$  state into the core level. Because of the dipole selection rules, apart from  $6s_{1/2}$  states (which have a small contribution to RIXS due to relatively small  $2p \rightarrow 6s$  matrix elements [50]) only  $5d_{3/2}$  states occur for  $L_2$  RIXS, whereas for  $L_3$  RIXS  $5d_{5/2}$ -states also contribute. Although the  $2p_{3/2} \rightarrow 5d_{3/2}$  radial matrix elements are only slightly smaller than the  $2p_{3/2} \rightarrow 5d_{5/2}$  ones, the angular matrix elements strongly suppress the  $2p_{3/2} \rightarrow 5d_{3/2}$  contribution [50]. Therefore, the RIXS spectrum at the Ir  $L_3$  edge can be viewed as interband transitions between  $5d_{5/2}$  states.

Figure 5 shows the experimental RIXS spectrum measured by Katukuri *et al.* [49] (open magenta circles) below 0.4 eV in comparison with the theoretical spectra calculated in the GGA+SO and GGA+SO+ $U$  approximations with different values of  $U_{\text{eff}}$ . The GGA+SO approach displays unsatisfactory agreement with the experiment. The best agreement was found for the GGA+SO+ $U$  approach with  $U_{\text{eff}} = 0.6$  eV. The calculations with larger  $U_{\text{eff}}$  shift the RIXS spectrum toward higher energies.

Figure 6(a) shows the theoretical RIXS spectrum at the Ir  $L_3$  edge for  $t_{2g} \rightarrow t_{2g}$  transitions in  $\text{Ba}_5\text{AlIr}_2\text{O}_{11}$  compared with different experimental data. The mea-

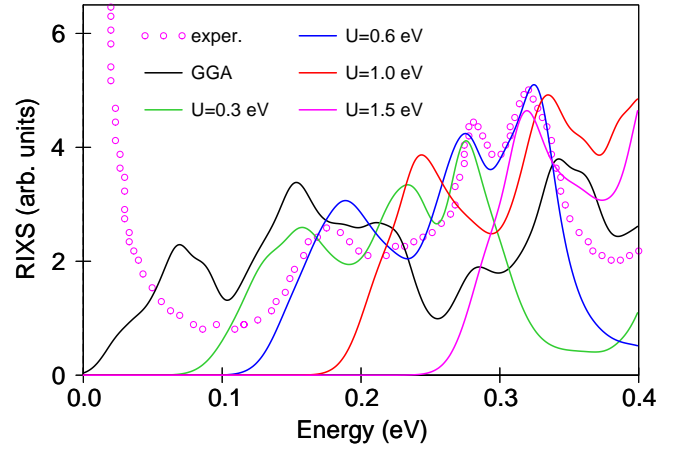


FIG. 5: (Color online) The experimentally measured RIXS spectrum at the Ir  $L_3$  edge [49] in  $\text{Ba}_5\text{AlIr}_2\text{O}_{11}$  compared with the theoretical spectra calculated in the GGA+SO+ $U$  approach for different  $U_{\text{eff}}$  values.

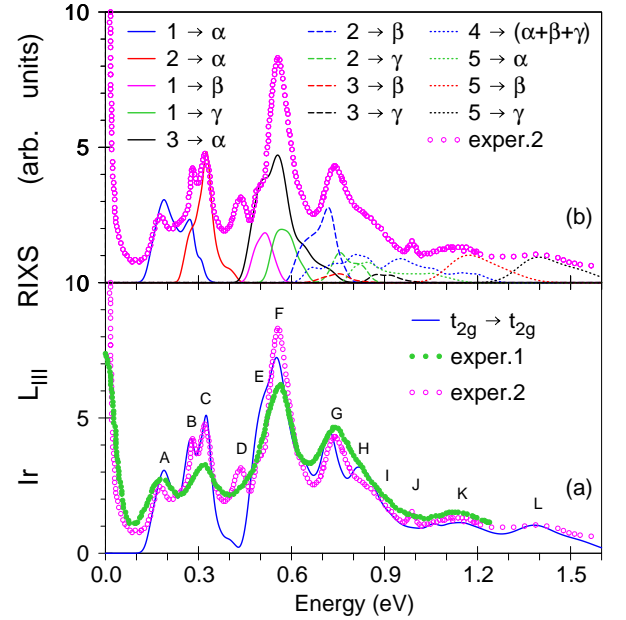


FIG. 6: (Color online) (a) The theoretical RIXS spectrum at the Ir  $L_3$  edge for  $t_{2g} \rightarrow t_{2g}$  transitions in  $\text{Ba}_5\text{AlIr}_2\text{O}_{11}$  (the full blue curve) calculated in the GGA+SO+ $U$  approach ( $U_{\text{eff}}=0.6$  eV) compared with different experimental data exper.1 [48] and exper.2 [49]; (b) the experimental RIXS spectrum at the Ir  $L_3$  edge for  $t_{2g} \rightarrow t_{2g}$  transitions in  $\text{Ba}_5\text{AlIr}_2\text{O}_{11}$  (magenta open circles) [49] in comparison with the interband transitions between  $t_{2g}$  states marked in Fig. 7.

surements by Wang *et al.* [48] (exper.1) and Katukuri *et al.* [49] (exper.2) produce quite similar RIXS spectra with just small differences in relative peak intensities. Additionally, exper.2 possesses an extra peak D and the low energy peak at  $\sim 0.3$  eV is split into two peaks B

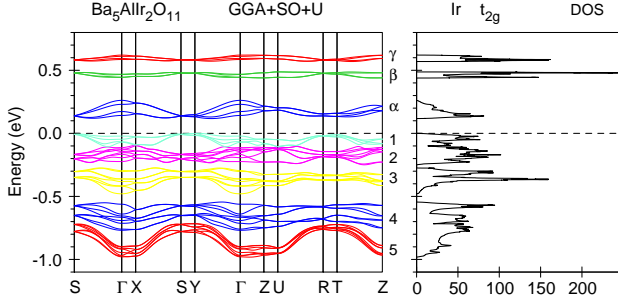


FIG. 7: (Color online) The energy band structure of the Ir  $t_{2g}$  states in  $\text{Ba}_5\text{AlIr}_2\text{O}_{11}$  calculated in the GGA+SO+ $U$  ( $U_{\text{eff}} = 0.6$  eV) approach.

and  $C$ . The Ir  $L_3$  spectrum for the  $t_{2g} \rightarrow t_{2g}$  transitions has quite a rich fine structure with at least twelve well separated peaks from  $A$  to  $L$  below 1.5 eV. This shape of the RIXS spectrum can be explained by the specific energy band structure of Ir  $t_{2g}$  states presented in Fig. 7. There are five separated groups of  $t_{2g}$  bands below  $E_F$  (from 1 to 5), and three groups of empty bands  $\alpha$ ,  $\beta$ , and  $\gamma$ , which produce three narrow DOS peaks separated by energy gaps. The interband transitions between these five occupied and three empty groups of bands produce 15 peaks (some of them are quite small). As a result, we have the rich structure of the Ir  $L_3$  RIXS spectrum consisting of twelve well distinguished peaks below 1.5 eV. The appearance of multiple peaks in the RIXS spectrum is a direct consequence of the strong noncubic crystal field splitting originating from the distorted octahedral environment of the Ir ions. The corresponding interband transitions are presented in Fig. 6(b). The low energy peaks  $A$ ,  $B$ , and  $C$  are due to transitions between the first (light green bands) and the second (magenta bands) groups of occupied bands into the low energy empty bands  $\alpha$  (blue bands). The peak  $D$  is absent in our calculations as well as in the measurements of Wang *et al.* [48] (exper.1). The peak probably has an excitonic nature, as it was suggested by Katukuri *et al.* [49]. This needs additional theoretical consideration. The theoretical description of exciton spectra demands a many-body approach beyond the one-particle approximation, such as GW or Bethe-Salpeter equation calculations. A first-principle approach for the description of exciton spectra with the consideration of RIXS matrix elements is highly desirable.

The intensive peak  $F$  at 0.55 eV with the low energy shoulder  $E$  is derived from  $1 \rightarrow \beta$ ,  $1 \rightarrow \gamma$  and  $3 \rightarrow \alpha$  interband transitions. The peak  $G$  is mostly due to  $2 \rightarrow \beta$  interband transitions. The high energy peaks  $K$  and  $L$  are due to  $5 \rightarrow \beta$  and  $5 \rightarrow \gamma$  interband transitions, respectively. The shoulders  $H$ ,  $I$ , and  $J$  occur from the combination of many transitions such as  $4 \rightarrow (\alpha + \beta + \gamma)$  and  $5 \rightarrow \alpha$  [see Fig. 6(b)].

Figure 8 (the lower panel) shows the experimental RIXS spectrum (open magenta circles) measured by

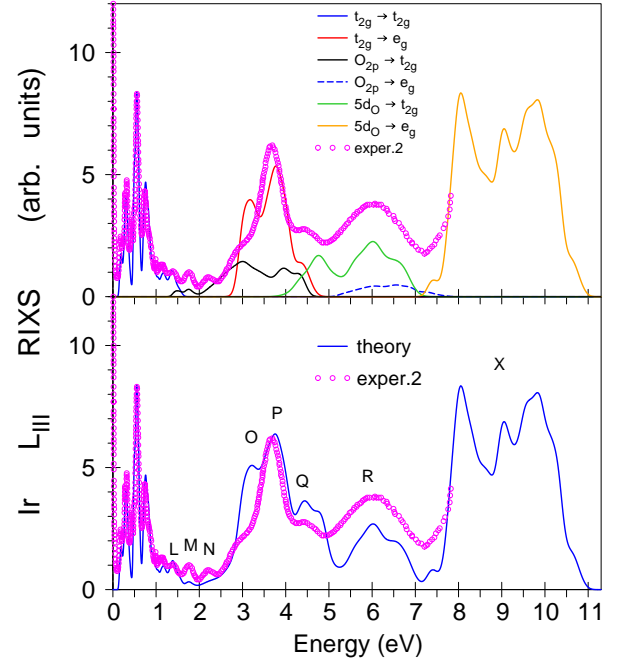


FIG. 8: (Color online) Lower panel: the experimental RIXS spectrum (open magenta circles) measured by Katukuri *et al.* [49] for the momentum transfer vector  $\mathbf{Q} = (23.5, 0, 2.5)$  in reciprocal lattice units and incident photon energy  $E_i = 11215$  eV at the Ir  $L_3$  edge in  $\text{Ba}_5\text{AlIr}_2\text{O}_{11}$  compared with the theoretically calculated one in the GGA+SO+ $U$  approach ( $U_{\text{eff}} = 0.6$  eV). Upper panel: the experimental RIXS spectrum (open magenta circles) measured by Katukuri *et al.* [49] at the Ir  $L_3$  edge and the decomposition of the Ir  $L_3$  RIXS spectrum into different interband transitions.

Katukuri *et al.* [49] at the Ir  $L_3$  edge in  $\text{Ba}_5\text{AlIr}_2\text{O}_{11}$  in a wide energy interval up to 8 eV compared with the theoretically calculated one in the GGA+SO+ $U$  approach. As we mentioned above, the interband transitions below 1.5 eV (the blue curve in the upper panel of Fig. 8) are due to the  $t_{2g} \rightarrow t_{2g}$  transitions. The intensive peak  $P$  at  $\sim 3.5$  eV with the low energy shoulder  $O$  is mostly due to  $t_{2g} \rightarrow e_g$  transitions (the red curve in the upper panel of Fig. 8). The  $\text{O}_{2p} \rightarrow t_{2g}$  transitions (the black curve in the upper panel of Fig. 8) also contribute to this peak and the low energy shoulder  $O$  as well as to small peaks  $M$  and  $N$ . The next fine structure  $R$  from 5 to 7 eV is due to  $5d_O \rightarrow t_{2g}$  transitions (the green curve). The shoulder  $Q$  is partly due to the  $5d_O \rightarrow t_{2g}$  transitions as well as due to the  $t_{2g} \rightarrow e_g$  transitions. The  $\text{O}_{2p} \rightarrow e_g$  transitions are very weak (the dashed blue curve). The high energy intensive peak  $X$  between 7.5 and 11 eV is due to  $5d_O \rightarrow e_g$  interband transitions.

It is widely believed that  $d-d$  excitations show only small momentum transfer vector  $\mathbf{Q}$  dependence in  $5d$  transition metal compounds. Figure 9(a) shows the RIXS spectra at the Ir  $L_3$  edge in  $\text{Ba}_5\text{AlIr}_2\text{O}_{11}$  calculated as a function of  $Q_x$  with the momentum transfer vector  $\mathbf{Q} = (Q_x, 0, 2.5)$  for incident photon energy  $\hbar\omega_{in} = 11215$  eV.



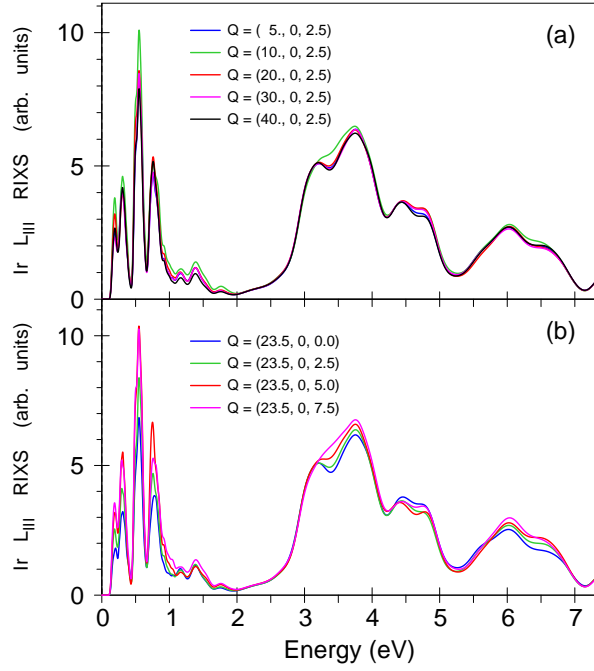


FIG. 9: (Color online) The RIXS spectra at the Ir  $L_3$  edge in  $\text{Ba}_5\text{AlIr}_2\text{O}_{11}$  calculated as a function of  $Q_x$  (a) and  $Q_z$  (b) with the momentum transfer vector  $\mathbf{Q} = (Q_x, 0, Q_z)$  in reciprocal lattice units for incident photon energy  $\hbar\omega_{in} = 11215$  eV.

We found that the RIXS spectra are quite similar for  $Q_x$  changing from 5 to 40 in reciprocal lattice units. With increasing  $Q_z$  for the momentum transfer vector  $\mathbf{Q} = (23.5, 0, Q_z)$ , the low energy peaks below 1.5 eV are slightly increased while the high energy fine structures between 2 and 7 eV are changed insignificantly [Fig. 9(b)].

Analyzing Fig. 9 we can conclude that the momentum dependence of the excitations in  $\text{Ba}_5\text{AlIr}_2\text{O}_{11}$  is rather small, as it was earlier observed in other iridates such as  $\text{Sr}_3\text{CuIrO}_6$  [70],  $\text{In}_2\text{Ir}_2\text{O}_7$  [71], or  $\text{Sr}_2\text{IrO}_4$  [68].

Figure 10 shows the Ir  $L_3$  RIXS spectrum as a function of incident photon energy  $E_i$  above the corresponding edge with the momentum transfer vector  $\mathbf{Q} = (23.5, 0, 2.5)$ . We found that the low energy fine structure  $\leq 1.5$  eV corresponding to intra- $t_{2g}$  excitations is steadily decreased when the incident photon energy changes from 11215 to 11223 eV, whereas the high energy peak corresponding to the  $t_{2g} \rightarrow e_g$  transitions shows more complex behavior. The intensity of the peak is increased with  $E_i$  varying from 11215 to 11219 eV, but then the peak is decreased with  $E_i$  increasing to 11221 and 11223 eV.

### C. RIXS spectra at the Ir $K$ and $M_5$ edges

Let us consider now the RIXS spectra at the Ir  $K$  and  $M_5$  edges. For that we first present in Fig. 11 the Ir  $6p$  (the lower panel) and  $5f$  (the upper panel) partial DOS

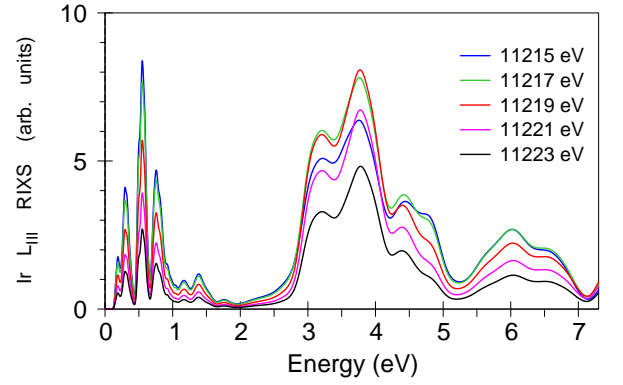


FIG. 10: (Color online) The RIXS spectra as a function of incident photon energy  $E_i$  calculated at the Ir  $L_3$  edge in  $\text{Ba}_5\text{AlIr}_2\text{O}_{11}$  with the momentum transfer vector  $\mathbf{Q} = (23.5, 0, 2.5)$  in reciprocal lattice units calculated in the GGA+SO+ $U$  approach ( $U_{\text{eff}} = 0.6$  eV).

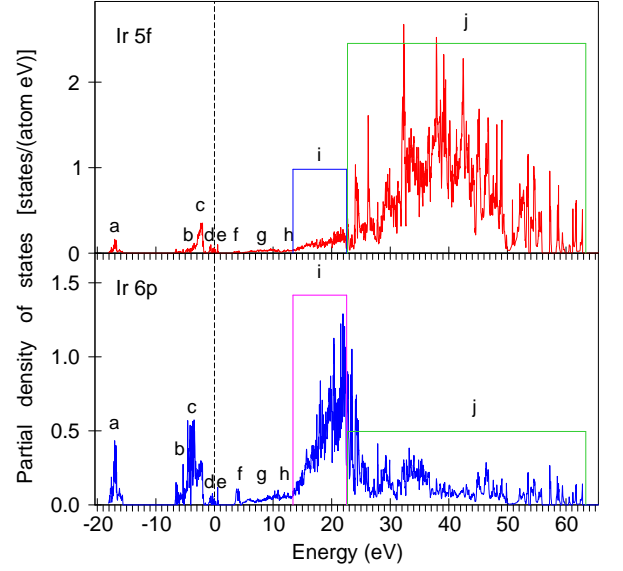


FIG. 11: (Color online) The Ir  $6p$  (the lower panel) and  $5f$  (the upper panel) partial DOS [in states/(atom eV)] in  $\text{Ba}_5\text{AlIr}_2\text{O}_{11}$  calculated in the GGA+SO+ $U$  ( $U_{\text{eff}} = 0.6$  eV) approach.

in a wide energy interval from  $-21$  to  $62$  eV. We distinguish several groups of bands. The group  $a$  derives from the hybridizations of Ir  $6p$  and  $5f$  states with oxygen  $2s$  states. The groups  $b$  and  $c$  are due to the hybridization of these states with oxygen  $2p$  states. The groups  $d$  and  $e$  are from the hybridization with Ir  $t_{2g}$  LEB and UEB, respectively. The group  $f$  comes from the hybridization with Ir  $e_g$  states. The group  $g$  comes from the hybridization with Ba  $5d$  and  $4f$  states, and the group  $h$  is due to the hybridization with Al  $3p$  states. The structure  $i$  is the Ir  $6p$  band itself. The structure  $j$  is the Ir  $5f$  band.

Figure 12(a) presents the theoretically calculated Ir  $K$

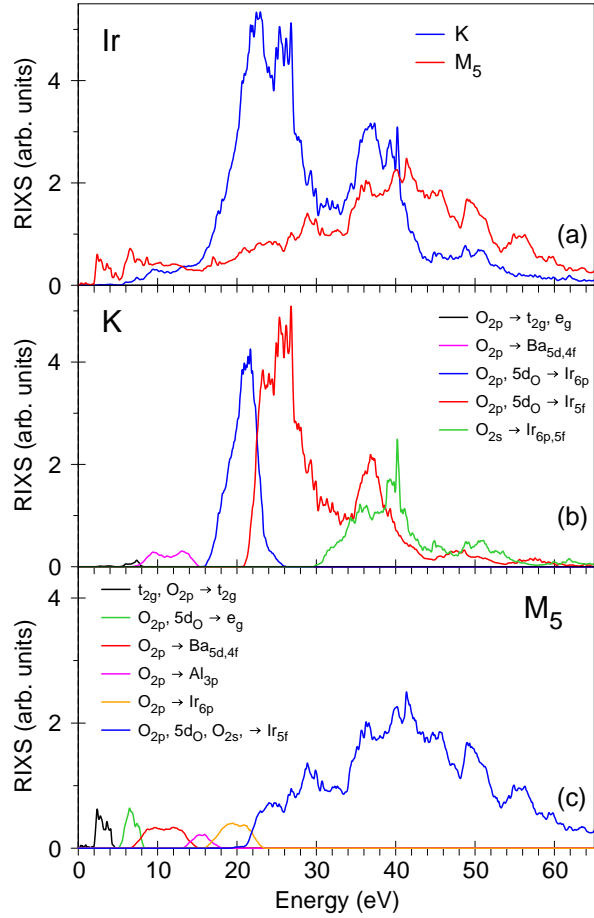


FIG. 12: (Color online) (a) The theoretically calculated RIXS spectrum at the Ir *K* (the blue curve) and *M*<sub>5</sub> (the red curve) edges in Ba<sub>5</sub>AlIr<sub>2</sub>O<sub>11</sub>; (b) the decomposition of the Ir *K* RIXS spectrum into different interband transitions; (c) the decomposition of the Ir *M*<sub>5</sub> RIXS spectrum into different interband transitions.

(the blue curve) and Ir *M*<sub>5</sub> (the red curve) RIXS spectra in Ba<sub>5</sub>AlIr<sub>2</sub>O<sub>11</sub>. The spectra significantly differ from each other and from the RIXS spectra at the Ir *L*<sub>3</sub> edge. The partial contributions from different interband transitions are presented in Figs. 12(b) and 12(c) for the Ir *K* and *M*<sub>5</sub> edges, respectively. Due to significantly smaller spatial localization of the Ir 5*f* orbitals in comparison with the 6*p* ones the peaks *a*, *b*, *c*, *d*, and *e*, which originate from the hybridization with oxygen 2*s* and 2*p*, and Ir *t*<sub>2*g*</sub> and *e*<sub>*g*</sub> states, respectively, possess much smaller intensity in the Ir 5*f* partial DOS in comparison with the Ir 6*p* one (Fig. 11). However, the low energy part of the Ir *M*<sub>5</sub> spectrum ≤10 eV possesses larger intensity in comparison with the Ir *K* RIXS spectrum due to the corresponding matrix elements. This part of the *M*<sub>5</sub> spectrum is due to (*t*<sub>2*g*</sub>, O<sub>2*p*</sub>, Ir5*d*<sub>O</sub>) → (*t*<sub>2*g*</sub>, *e*<sub>*g*</sub>) transitions. The major contribution to the Ir *M*<sub>5</sub> RIXS spectrum above 20 eV is due to the interband transitions into Ir 5*f* states [the blue curve in Fig. 12(c)].

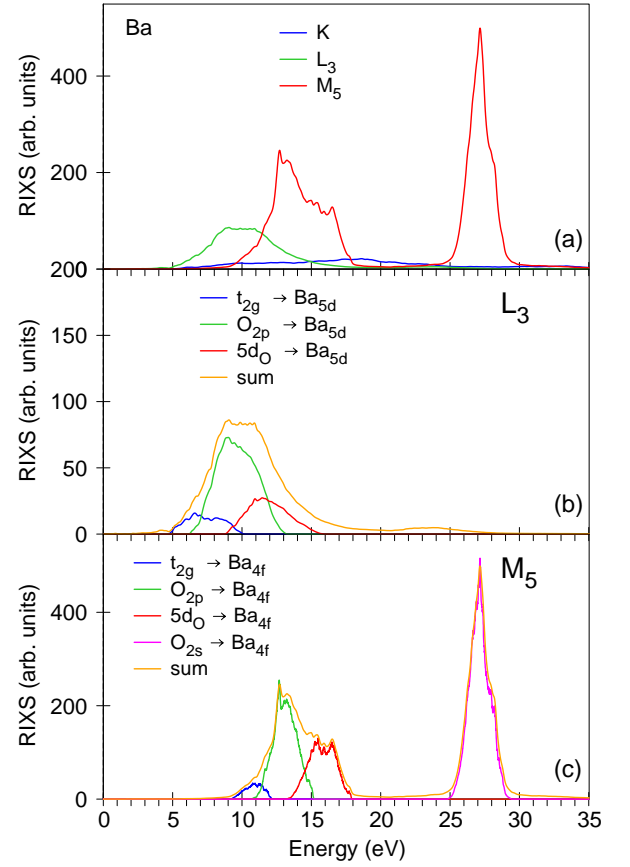


FIG. 13: (Color online) (a) The theoretically calculated RIXS spectrum at the Ba *K* (the blue curve), *L*<sub>3</sub> (the green curve), and *M*<sub>5</sub> (the red curve) edges in Ba<sub>5</sub>AlIr<sub>2</sub>O<sub>11</sub>; (b) the decomposition of the Ba *L*<sub>3</sub> RIXS spectrum into different interband transitions; (c) the decomposition of the Ba *M*<sub>5</sub> RIXS spectrum into different interband transitions.

The Ir *K* RIXS spectrum consists of two major peaks at 8-30 and 32-44 eV. The low energy part of the first peak is due to the interband transitions from O<sub>2*p*</sub> and 5*d*<sub>O</sub> states into empty Ir<sub>6*p*</sub> states [the blue curve in Fig. 12(b)]. The transitions (O<sub>2*p*</sub>, 5*d*<sub>O</sub>) → Ir<sub>5*f*</sub> contribute to both peaks [the red curve in Fig. 12(b)]. We can also see a visible contribution into the second peak at 32-44 eV of O<sub>2*s*</sub> → Ir<sub>6*p,5f*</sub> transitions (the green curve). Experimental measurements of the RIXS spectra at the Ir *K* and *M*<sub>5</sub> edges are highly desirable.

#### D. RIXS spectra at the Ba *K*, *L*<sub>3</sub>, and *M*<sub>5</sub> edges

Figure 13(a) presents the theoretically calculated Ba *K* (the blue curve), *L*<sub>3</sub> (the green curve) and *M*<sub>5</sub> (the red curve) RIXS spectra in Ba<sub>5</sub>AlIr<sub>2</sub>O<sub>11</sub>. These spectra significantly differ from each other and from the RIXS spectra at the Ir *K*, *L*<sub>3</sub>, and *M*<sub>5</sub> edges. The partial contributions from different interband transitions are presented in Figs. 13(b) and 13(c) for the Ba *L*<sub>3</sub> and *M*<sub>5</sub>

edges, respectively.

The Ba  $M_5$  RIXS spectrum is the most intensive and consists of two peaks separated by a rather wide energy gap: a low energy peak between 9 and 18 eV and a high energy narrow peak at 25–29 eV. The latter peak is completely due to  $O_{2s} \rightarrow Ba_{4f}$  transitions [the magenta curve in Fig. 13(c)]. The low energy peak is devoted to the interband transitions from  $t_{2g}$ ,  $O_{2p}$ , and  $5d_O$  states into  $Ba_{4f}$  ones. The Ba  $L_3$  RIXS spectrum possesses a single peak between 5 and 16 eV, which is formed by the transitions from the  $t_{2g}$ ,  $O_{2p}$ , and  $5d_O$  states into Ba  $5d$  states [see Fig. 13(b)]. The Ba  $K$  RIXS spectrum possesses relatively small intensity and is formed by the interband transitions from  $O_{2s}$ ,  $O_{2p}$ , and  $5d_O$  states into Ba  $5d$ ,  $4f$ , Al  $3p$ , and Ir  $6p$  states with almost equal intensity (not shown). Experimental measurements of the RIXS spectra at the Ba  $K$ ,  $L_3$  and  $M_5$  edges could be quite perspective and are highly desirable.

### E. XAS and RIXS spectra at the O $K$ edge

In the XAS, XMCD, and RIXS processes at the O  $K$  edge, the  $1s$  core level is involved. The exchange splitting of the  $1s$ -core state is extremely small and SOC is absent for O  $1s$  orbitals, therefore, only the exchange and spin-orbit splitting of the  $2p$  states is responsible for the observed spectra at the oxygen  $K$  edge. However, the oxygen valence  $2p$  states because of their delocalized nature are sensitive to the electronic states at neighboring  $5d$  sites. They strongly hybridize with the  $5d$  orbitals. Due to such hybridization combined with high SOC at the  $5d$  ion, information on the elementary excitations can be extracted using an indirect RIXS process at the O  $K$  edge [72]. Although O  $K$  RIXS has a much smaller penetration depth ( $\sim 100$  nm) than  $5d L$  RIXS, a comparison between O  $K$  and Ir  $L_3$  spectra measured, for example, for  $Sr_2IrO_4$  suggests that they have comparable counting efficiency [72]. The lower penetration depth of soft x-rays has its own advantages providing high sensitivity to ultrathin samples such as films. Soft x-ray RIXS at the O  $K$  edge is a promising method for studying the electronic and magnetic excitations in  $5d$  compounds. The RIXS spectra as well as XAS spectra at the oxygen  $K$  edge in  $Ba_5AlIr_2O_{11}$  were investigated experimentally by Katukuri *et al.* [49] for different polarizations.

Figure 14 presents the RIXS spectra in  $Ba_5AlIr_2O_{11}$  measured by Katukuri *et al.* [49] at the O  $K$  edge for grazing incidence and excitation energy  $E_i = 527.6$  eV with the momentum transfer vector  $\mathbf{Q} = (0.93, 0, 0.65)$  for the  $\sigma$  (open green circles in the lower panel) and  $\pi$  (open magenta circles in the upper panel) polarizations in comparison with the spectra calculated in the GGA+SO+ $U$  approach. The O  $K$  RIXS spectra consist of the elastic peak centered at zero energy loss and three major inelastic excitations  $\leq 1$  eV, 1.8–4.7 eV, and  $> 5$  eV. We found that the low energy features  $\leq 1$  eV (the blue curves in Fig. 14) are due to the interband tran-

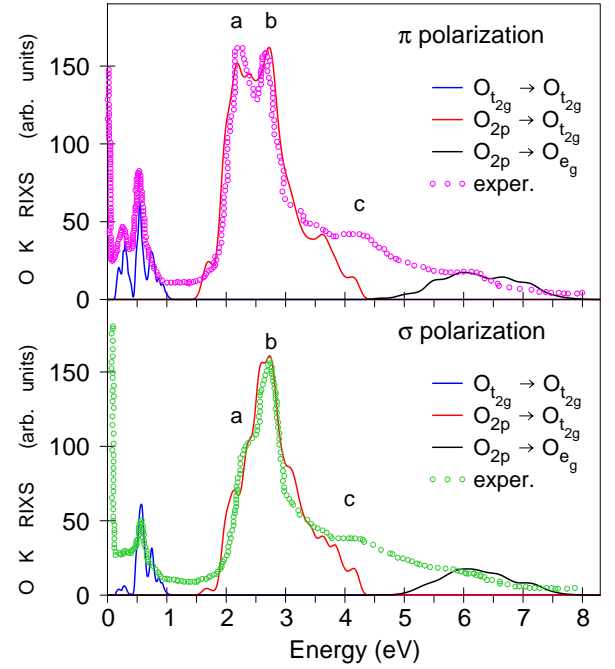


FIG. 14: (Color online) The RIXS spectra in  $Ba_5AlIr_2O_{11}$  measured by Katukuri *et al.* [49] at the O  $K$  edge for grazing incidence and excitation energy  $E_i = 527.6$  eV with the momentum transfer vector  $\mathbf{Q} = (0.93, 0, 0.65)$  in reciprocal lattice units for the  $\sigma$  (open green circles in the lower panel) and  $\pi$  (open magenta circles in the upper panel) polarizations in comparison with the spectra calculated in the GGA+SO+ $U$  ( $U_{\text{eff}} = 0.6$  eV) approach.

sitions between occupied and empty  $O_{t_{2g}}$  states, which appear as a result of the strong hybridization between oxygen  $2p$  states with Ir  $t_{2g}$  LEB and UEB in close vicinity to the Fermi level (Fig. 3). The next major fine structures between 1.8 and 4.7 eV (the red curves in Fig. 14) consist of two peaks *a* and *b* and a high energy shoulder *c*. These fine structures reflect the interband transitions from occupied O  $2p$  states to empty oxygen states, which originate from the hybridization with Ir  $t_{2g}$  states. The peak *a* is significantly suppressed for the  $\sigma$  polarization in comparison with the  $\pi$  one. The theory reproduces well the shapes and energy positions and relative intensity of the low energy features *a* and *b* for both polarizations, but not the high energy shoulder *c*, which is underestimated in our calculations. The  $O_{2p} \rightarrow e_g$  transitions situated between 5 and 8 eV energy interval (the black curves in Fig. 14) have quite small intensity and appear in the experimental spectrum just as a tail.

Figure 15 presents the RIXS spectra as a function of incident photon energy  $E_i$  calculated at the O  $K$  edge in  $Ba_5AlIr_2O_{11}$  for two polarizations. We found much stronger dependence on the incident photon energy in the case of the O  $K$  RIXS spectrum in comparison with the corresponding dependence at the Ir  $L_3$  edge (compare Figs. 10 and 15). With increasing the incident photon

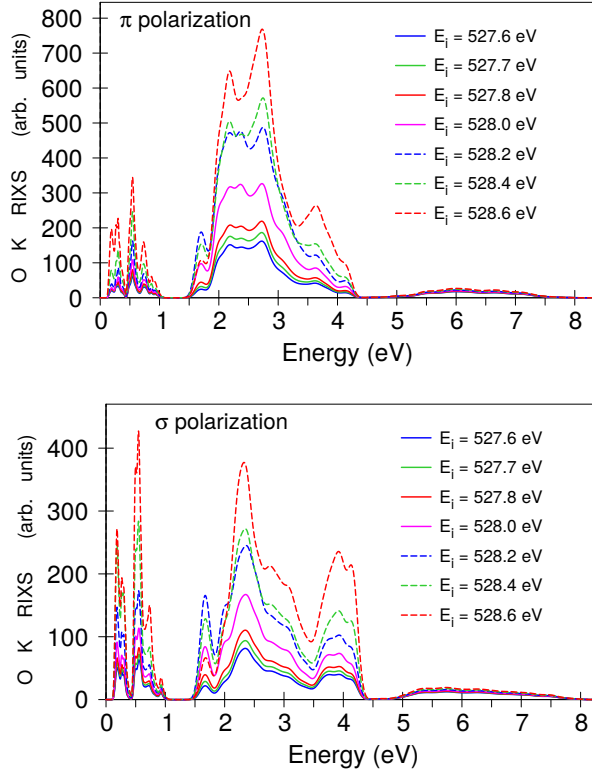


FIG. 15: (Color online) The RIXS spectra at the O  $K$  edge as a function of incident photon energy for the  $\sigma$  (the lower panel) and  $\pi$  (the upper panel) polarizations calculated in the GGA+SO+ $U$  ( $U_{\text{eff}}=0.6$  eV) approach.

energy both the peaks  $\leq 1$  eV and the peaks between 1.8 and 4.7 eV are significantly increased for both polarizations. This occurs in a small energy interval of 1 eV for  $E_i$  from 527.6 to 528.6 eV. However, the  $O_{2p} \rightarrow e_g$  inter-band transitions, situated in the 5–8 eV energy interval, possess quite small incident photon energy dependence for both polarizations.

Figure 16(a) shows the RIXS spectra at the O  $K$  edge in  $\text{Ba}_5\text{AlIr}_2\text{O}_{11}$  calculated as a function of  $Q_x$  with the momentum transfer vector  $\mathbf{Q} = (Q_x, 0, 2.5)$  for incident photon energy  $\hbar\omega_{in} = 527.6$  eV and the  $\sigma$  polarization. We found that the  $t_{2g} \rightarrow t_{2g}$  transitions at  $\leq 1$  eV energy interval as well as the  $O_{2p} \rightarrow t_{2g}$  transitions between 1.8 and 4.5 eV are monotonously increased for  $Q_x$  changing from 5 to 30 in reciprocal lattice units, while the  $O_{2p} \rightarrow e_g$  transitions between 5 and 8 eV are changed insignificantly. With increasing  $Q_z$ , the low energy peaks  $\leq 1$  eV are changed insignificantly [for the momentum transfer vector  $\mathbf{Q} = (23.5, 0, Q_z)$ ] and the high energy fine structures between 1.8 and 4.5 eV are decreased [Fig. 16(b)]. The  $O_{2p} \rightarrow e_g$  transitions are less sensitive to the momentum transfer vector  $\mathbf{Q}$ .

Figure 17 presents the experimental O  $K$  XAS spectra for the  $\pi$  (open magenta circles in the upper panel) and  $\sigma$  polarizations (open green circles in the lower panel) [49]

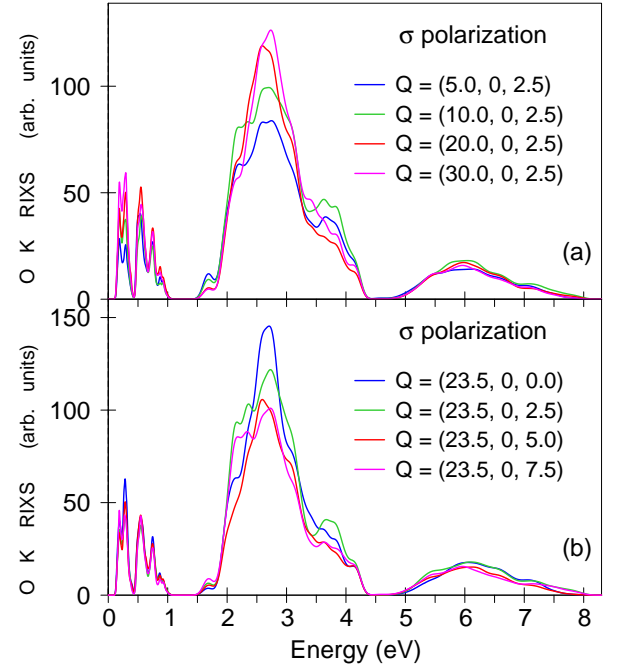


FIG. 16: (Color online) The RIXS spectra at the O  $K$  edge in  $\text{Ba}_5\text{AlIr}_2\text{O}_{11}$  calculated as a function of  $Q_x$  (a) and  $Q_z$  (b) with the momentum transfer vector  $\mathbf{Q} = (Q_x, 0, Q_z)$  in reciprocal lattice units for incident photon energy  $\hbar\omega_{in} = 527.6$  eV.

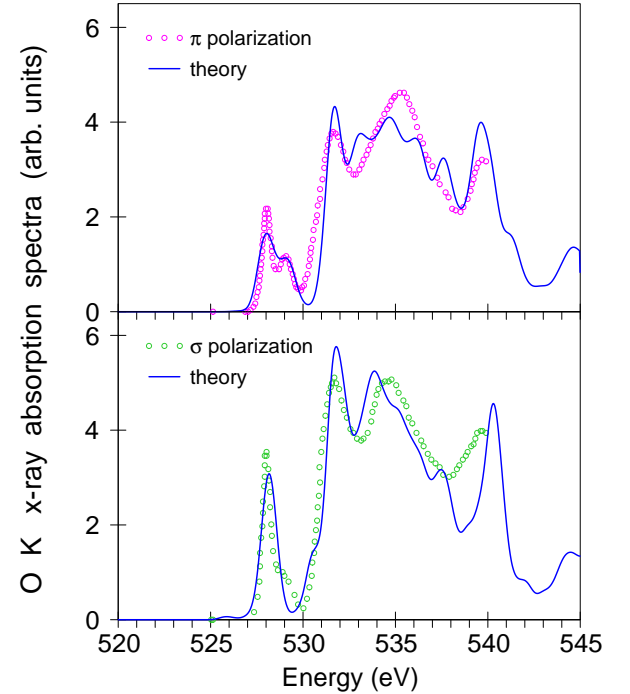


FIG. 17: (Color online) The experimental O  $K$  polarization-dependent XAS spectra (open circles) [49] in  $\text{Ba}_5\text{AlIr}_2\text{O}_{11}$  compared with the theoretically calculated ones in the GGA+SO+ $U$  approach ( $U_{\text{eff}} = 0.6$  eV).

compared with the theoretically calculated ones in the GGA+SO+ $U$  approach. The theory reproduces quite well the polarization dependence of the O  $K$  XAS spectrum. There is a single quite intensive low energy peak at 528 eV for the  $\sigma$  polarization. The corresponding peak for the  $\pi$  polarization is split into two peaks with relatively smaller intensity. Although the theory reproduces relatively well the shape of the peak at 530-538 eV for the  $\sigma$  polarization, for the  $\pi$  polarization our calculations show several peaks at 533-539 eV instead of one as in the experiment.

## V. CONCLUSIONS

To summarize, we have investigated the electronic and magnetic structures of  $\text{Ba}_5\text{AlIr}_2\text{O}_{11}$  in the frame of the fully relativistic spin-polarized Dirac approximation. We also present comprehensive theoretical calculations of the RIXS spectra at the Ir  $K$ ,  $L_3$ ,  $M_5$ , Ba  $K$ ,  $L_3$ ,  $M_5$  and oxygen  $K$  edges, the XAS and XMCD spectra at the Ir  $L_{2,3}$  edges, and polarization dependence of the O  $K$  XAS spectra.

$\text{Ba}_5\text{AlIr}_2\text{O}_{11}$  is a Mott insulator that undergoes a subtle structural phase transition near  $T_S = 210$  K and a transition to FiM order at  $T_M = 4.5$  K. The GGA+SO band structure calculations produce a metallic solution for  $\text{Ba}_5\text{AlIr}_2\text{O}_{11}$  in contradiction to experiment. To produce the correct dielectric ground state one has to take into account strong Coulomb correlations in  $\text{Ba}_5\text{AlIr}_2\text{O}_{11}$ . The crystal structure of  $\text{Ba}_5\text{AlIr}_2\text{O}_{11}$  consists of  $\text{IrO}_6$  octahedra sharing a face along the crystallographic  $b$  axis, and develop so called  $\text{Ir}_2\text{O}_9$  dimers. Each dimer consists of two inequivalent octahedral  $\text{Ir}_1$  and  $\text{Ir}_2$  sites. It was supposed that  $\text{Ba}_5\text{AlIr}_2\text{O}_{11}$  possesses charge order with  $\text{Ir}_1$  and  $\text{Ir}_2$  sites occupied by pentavalent  $\text{Ir}^{5+}$  ( $5d^4$ ) and tetravalent  $\text{Ir}^{4+}$  ( $5d^5$ ) ions, respectively. However, we have found that the charge disproportionation of  $\sim 0.3$  electron is not complete. A purely ionic model with strong SOC, which would support  $J_{\text{eff}} = \frac{1}{2}$  in the  $\text{Ir}_2^{4+}$  ( $5d^5$ ) ions and  $J_{\text{eff}} = 0$  in the  $\text{Ir}_1^{5+}$  ( $5d^4$ ) ions, is not entirely applicable in  $\text{Ba}_5\text{AlIr}_2\text{O}_{11}$ . Our GGA+SO+ $U$  calculations produce the ionicity equal to +4.3 and +4.7 for  $\text{Ir}_2$  and  $\text{Ir}_1$ , respectively.

The remarkably large branching ratio  $\text{BR} = I_{L_3}/I_{L_2} = 4.09$  and  $3.70$  for the  $\text{Ir}_2$  and  $\text{Ir}_1$  sites, respectively, indicates strong SO effects in  $\text{Ba}_5\text{AlIr}_2\text{O}_{11}$ . There is a relatively large XMCD signal at the  $L_3$  edge for the  $\text{Ir}_2$  site. However, for the  $\text{Ir}_1$  site the dichroism is much smaller due to the smallness of the orbital magnetic moment at that site.

The theoretically calculated Ir  $L_3$  RIXS spectrum is in good agreement with the experiment. We have found that the low energy peaks  $\leq 1.5$  eV correspond to intra- $t_{2g}$  excitations. There are five separated groups of  $t_{2g}$  bands below  $E_F$  and three groups of empty bands, which produce three narrow DOS peaks separated by energy gaps. The interband transitions between these five occupied

and three empty groups of bands produce quite a rich fine structure of the Ir  $L_3$  RIXS spectrum consisting of twelve well distinguished peaks below  $\leq 1.5$  eV. The appearance of multiple peaks in the RIXS spectrum is a direct consequence of the strong noncubic crystal field splitting originating from the distorted octahedral environment of the Ir ions. The intensive peak at  $\sim 3.5$  eV is mostly due to  $t_{2g} \rightarrow e_g$  transitions. The next fine structure from 4 to 7 eV is mostly due to  $5d_O \rightarrow t_{2g}$  transitions. The high energy intensive peak between 7.5 and 11 eV is due to  $5d_O \rightarrow e_g$  interband transitions.

We have found that the momentum dependence of the excitations in  $\text{Ba}_5\text{AlIr}_2\text{O}_{11}$  is rather small, as it was earlier observed in other iridates such as  $\text{Sr}_3\text{CuIrO}_6$ ,  $\text{In}_2\text{Ir}_2\text{O}_7$ , or  $\text{Sr}_2\text{IrO}_4$ . We have also investigated the Ir  $L_3$  RIXS spectrum as a function of incident photon energy  $E_i$  and found that the low energy fine structure corresponding to intra- $t_{2g}$  excitations is slightly decreased when the incident photon energy changes from 11210 to 11212 eV, whereas the high energy peak corresponding to the  $t_{2g} \rightarrow e_g$  transitions is monotonically increased.

The RIXS spectra at the Ir  $K$  and  $M_5$  edges occupy quite a wide energy interval up to 60 eV, which almost six times larger than, for example, the occupation interval of the Ir  $L_3$  or oxygen  $K$  spectra. The major contribution to the Ir  $M_5$  RIXS spectrum comes from the interband transitions into empty Ir  $5f$  bands. The Ir  $K$  spectrum reflects the energy distribution of different states in  $\text{Ba}_5\text{AlIr}_2\text{O}_{11}$  (oxygen  $2s$  and  $2p$ , Ir  $5d$  and  $5f$ ) due to the extended character of Ir  $6p$  orbitals. Experimental measurements of the RIXS spectra at the Ir  $K$  and  $M_5$  edges could be quite perspective.

Another useful possibility is the extension of the RIXS measurements on the Ba  $K$ ,  $L_3$ , and  $M_5$  edges. These spectra also significantly differ from each other and from the RIXS spectra at the Ir  $K$ ,  $L_3$ , and  $M_5$  edges. The Ba  $M_5$  RIXS spectrum is the most intensive and consists of two peaks separated by a rather wide energy gap: a low energy peak between 9 and 18 eV and a high energy narrow peak at 25–29 eV. The latter peak is completely due to  $\text{O}_{2s} \rightarrow \text{Ba}_{4f}$  transitions. The low energy peak is devoted to the interband transitions from  $t_{2g}$ ,  $\text{O}_{2p}$ , and  $5d_O$  states into  $\text{Ba}_{4f}$  ones. The Ba  $L_3$  RIXS spectrum possesses a single peak between 5 and 16 eV, which is formed by the transitions from the  $t_{2g}$ ,  $\text{O}_{2p}$ , and  $5d_O$  states into Ba  $5d$  states. The Ba  $K$  RIXS spectrum possesses relatively small intensity and is formed by the interband transitions from  $\text{O}_{2s}$ ,  $\text{O}_{2p}$ , and  $5d_O$  states into Ba  $5d$ ,  $4f$ , Al  $3p$ , and Ir  $6p$  states with almost equal intensity.

The RIXS spectrum of  $\text{Ba}_5\text{AlIr}_2\text{O}_{11}$  at the O  $K$  edge consists of three major inelastic excitations  $\leq 1$  eV, from 1.8 to 4.7 eV, and  $> 5$  eV. We have found that the first low energy feature is due to the interband transitions between occupied and empty  $\text{O}_{t_{2g}}$  states, which appear as a result of the strong hybridization between oxygen  $2p$  states with Ir  $t_{2g}$  LEB and UEB in the vicinity of the Fermi level. The next major structure from 1.8 to 4.7 eV reflects the interband transitions from occupied O  $2p$



states to empty oxygen states, which originate from the hybridization with Ir  $t_{2g}$  states. The  $O_{2p} \rightarrow e_g$  transitions are situated between 5 and 8 eV, have quite small intensity, and appear in the experimental spectrum just as a tail. The RIXS as well as XAS spectra at the oxygen  $K$  edge in  $Ba_5AlIr_2O_{11}$  show relatively strong polarization dependence.

We have found much stronger dependence on incident photon energy  $E_i$  at the O  $K$  edge than at the Ir  $L_3$  edge. With increasing the incident photon energy, the O  $K$  peaks  $\leq 1$  eV and between 1.8 and 4.7 eV are increased. This occurs in a small energy interval of 1 eV for  $E_i$  from 527.6 to 528.6 eV. However, the  $O_{2p} \rightarrow e_g$  interband transitions, situated in the 5–8 eV energy interval, possess quite small incident photon energy dependence

for both  $\sigma$  and  $\pi$  polarizations.

### Acknowledgments

We are thankful to Dr. Alexander Yaresko from the Max Planck Institute FKF in Stuttgart and Dr. Yuri Kucherenko from the G.V. Kurdyumov Institute for Metal Physics of the N.A.S. of Ukraine for helpful discussions.

The studies were supported by the National Academy of Sciences of Ukraine within the budget program KP-KBK 6541230 "Support for the development of priority areas of scientific research".

- 
- [1] B. J. Kim, H. Jin, S. J. Moon, J.-Y. Kim, B.-G. Park, C. S. Leem, J. Yu, T. W. Noh, C. Kim, S.-J. Oh, et al., *Phys. Rev. Lett.* **101**, 076402 (2008).
  - [2] B. J. Kim, H. Ohsumi, T. Komesu, S. Sakai, T. Morita, H. Takagi, and T. Arima, *Science* **323**, 1329 (2009).
  - [3] G. Jackeli and G. Khaliullin, *Phys. Rev. Lett.* **102**, 017205 (2009).
  - [4] G. Chen, R. Pereira, and L. Balents, *Phys. Rev. B* **82**, 174440 (2010).
  - [5] W. Witczak-Krempa, G. Chen, Y. B. Kim, and L. Balents, *Annu. Rev. Condens. Matter Phys.* **5**, 57 (2014).
  - [6] X.-L. Qi and S.-C. Zhang, *Physics Today* **63**, 33 (2010).
  - [7] Y. Ando, *J. Phys. Soc. Jpn.* **82**, 102001 (2013).
  - [8] T. O. Wehling, A. Black-Schafferc, and A. Balatsky, *Adv. Phys.* **63**, 1 (2014).
  - [9] A. Bansil, L. H. and T. Das, *Rev. Mod. Phys.* **88**, 021004 (2016).
  - [10] H. Watanabe, T. Shirakawa, and S. Yunoki, *Phys. Rev. Lett.* **105**, 216410 (2010).
  - [11] C. Martins, M. Aichhorn, L. Vaugier, and S. Biermann, *Phys. Rev. Lett.* **107**, 266404 (2011).
  - [12] W. Witczak-Krempa and Y. B. Kim, *Phys. Rev. B* **85**, 045124 (2012).
  - [13] A. Go, W. Witczak-Krempa, G. S. Jeon, K. Park, and Y. B. Kim, *Phys. Rev. Lett.* **109**, 066401 (2012).
  - [14] A. B. Sushkov, J. B. Hofmann, G. S. Jenkins, J. Ishikawa, S. Nakatsuji, S. DasSarma, and H. D. Drew, *Phys. Rev. B* **92**, 241108 (2015).
  - [15] I. Kimchi, J. G. Analytis, and A. Vishwanath, *Phys. Rev. B* **90**, 205126 (2014).
  - [16] I. I. Mazin, H. O. Jeschke, K. Foyevtsova, R. Valenti, and D. I. Khomskii, *Phys. Rev. Lett.* **109**, 197201 (2012).
  - [17] H.-S. Kim, C. H. Kim, H. Jeong, H. Jin, and J. Yu, *Phys. Rev. B* **87**, 165117 (2013).
  - [18] T. Takayama, A. Yaresko, A. Matsumoto, J. Nuss, K. Ishii, M. Yoshida, J. Mizuki, and H. Takagi, *Scientific Report* **4**, 6818 (2017).
  - [19] T. Takayama, A. Kato, R. Dinnebier, J. Nuss, H. Kono, L. S. I. Veiga, G. Fabbri, D. Haskel, and H. Takagi, *Phys. Rev. Lett.* **114**, 077202 (2015).
  - [20] L. S. I. Veiga, M. Etter, K. Glazyrin, F. Sun, J. C. A. Escanhoela, G. Fabbri, J. R. L. Mardegan, P. S. Malavi, Y. Deng, P. P. Stavropoulos, et al., *Phys. Rev. B* **96**, 140402(R) (2017).
  - [21] V. Hermann, M. Altmeyer, J. Ebad-Allah, F. Freund, A. Jesche, A. A. Tsirlin, M. Hanfland, P. Gegenwart, I. I. Mazin, D. I. Khomskii, et al., *Phys. Rev. B* **97**, 020104(R) (2018).
  - [22] V. N. Antonov, L. V. Bekenov, and D. A. Kukusta, *Phys. Rev. B* **102**, 195134 (2020).
  - [23] V. N. Antonov, D. A. Kukusta, L. Uba, A. Bonda, and S. Uba, *Phys. Rev. B* **103**, 235127 (2021).
  - [24] V. N. Antonov, S. Uba, and L. Uba, *Phys. Rev. B* **98**, 245113 (2018).
  - [25] G.-W. Chern and C. D. Batista, *Phys. Rev. Lett.* **107**, 186403 (2011).
  - [26] Q. Chen, C. Svoboda, Q. Zheng, B. C. Sales, D. G. Mandrus, H. D. Zhou, J.-S. Zhou, D. McComb, M. Randeria, N. Trivedi, et al., *Phys. Rev. B* **96**, 144423 (2017).
  - [27] A. Earnshaw, B. Figgis, J. Lewis, and R. Peacock, *J. Chem. Soc. (Resumed)* **0**, 3132 (1961).
  - [28] G. Cao, T. F. Qi, L. Li, J. Terzic, S. J. Yuan, L. E. DeLong, G. Murthy, and R. K. Kaul, *Phys. Rev. Lett.* **112**, 056402 (2014).
  - [29] G. Khaliullin, *Phys. Rev. Lett.* **111**, 197201 (2013).
  - [30] J. Terzic, J. C. Wang, F. Ye, W. H. Song, S. J. Yuan, S. Aswartham, L. E. DeLong, S. V. Streltsov, D. I. Khomskii, and G. Cao, *Phys. Rev. B* **91**, 235147 (2015).
  - [31] G. Cao and L. E. DeLong, *Frontiers of 4d- and 5d-Transition Metal Oxides* (World Scientific, Singapore, 2013).
  - [32] M. Imada, A. Fujimori, and Y. Tokura, *Rev. Mod. Phys.* **30**, 1039 (1998).
  - [33] H. F. Pen, J. van den Brink, D. I. Khomskii, and G. A. Sawatzky, *Phys. Rev. Lett.* **78**, 1323 (1997).
  - [34] D. I. Khomskii and T. Mizokawa, *Phys. Rev. Lett.* **94**, 156402 (2005).
  - [35] S. Ogawa, *J. Phys. Soc. Jpn.* **15**, 1901 (1960).
  - [36] M. A. McGuire, J. Yan, P. Lampen-Kelley, A. F. May, V. R. Cooper, L. Lindsay, A. Piretzky, L. Liang, S. KC, E. Cakmak, et al., *Phys. Rev. Mater.* **1**, 064001 (2017).
  - [37] Y. Miura, Y. Yasui, M. Sato, N. Igawa, and K. Kakurai, *J. Phys. Soc. Jpn.* **76**, 033705 (2007).
  - [38] G. Bastien, G. Garbarino, R. Yadav, F. J. Martinez-Casado, R. B. Rodriguez, Q. Stahl, M. Kusch, S. P. Limandri, R. Ray, P. Lampen-Kelley, et al., *Phys. Rev. B*

- 97**, 241108(R) (2018).
- [39] T. Biesner, S. Biswas, W. Li, Y. Saito, A. Pustogow, M. Altmeyer, A. U. B. Wolter, B. Büchner, M. Roslova, T. Doert, et al., Phys. Rev. B **97**, 220401(R) (2018).
  - [40] T. Takayama, A. Krajewska, A. S. Gibbs, A. N. Yaresko, H. Ishii, H. Yamaoka, K. Ishii, N. Hiraoka, N. P. Funnell, C. L. Bull, et al., Phys. Rev. B **99**, 125127 (2019).
  - [41] I. Terasaki, S. Ito, T. Igarashi, S. Asai, H. Taniguchi, R. Okazaki, Y. Yasui, K. Kobayashi, R. Kumai, H. Nakao, et al., Crystals **6**, 27 (2016).
  - [42] A. Nag, S. Middey, S. Bhowal, S. K. Panda, R. Mathieu, J. C. Orain, F. Bert, P. Mendels, P. G. Freeman, M. Mansson, et al., Phys. Rev. Lett. **116**, 097205 (2016).
  - [43] T. Dey, M. Majumder, J. C. Orain, A. Senyshyn, M. Prinz-Zwick, S. Bachus, Y. Tokiwa, F. Bert, P. Khuntia, N. Büttgen, et al., Phys. Rev. B **96**, 174411 (2017).
  - [44] A. Nag, S. Bhowal, F. Bert, A. D. Hillier, M. Itoh, I. Carlomagno, C. Meneghini, T. Sarkar, R. Mathieu, I. Dasgupta, et al., Phys. Rev. B **97**, 064408 (2018).
  - [45] C.-C. Kao, W. A. L. Caliebe, J. B. Hastings, and J.-M. Gillet, Phys. Rev. B **54**, 16361 (1996).
  - [46] L. J. P. Ament, M. van Veenendaal, T. P. Devereaux, J. P. Hill, and J. van den Brink, Rev. Mod. Phys. **83**, 705 (2011).
  - [47] F. M. F. de Groot, M. W. Haverkort, H. Elnaggar, A. Juhin, K.-J. Zhou, and P. Glatzel, Nat. Rev. Methods Primers **4**, 46 (2024).
  - [48] Y. Wang, R. Wang, J. Kim, M. H. Upton, D. Casa, T. Gog, G. Cao, G. Kotliar, M. P. M. Dean, and X. Liu, Phys. Rev. Lett. **122**, 106401 (2019).
  - [49] V. M. Katukuri, X. Lu, D. E. McNally, M. Dantz, V. N. Strocov, M. M. Sala, M. H. Upton, J. Terzic, G. Cao, O. V. Yazyev, et al., Phys. Rev. B **105**, 075114 (2022).
  - [50] V. Antonov, B. Harmon, and A. Yaresko, *Electronic Structure and Magneto-Optical Properties of Solids* (Kluwer, Dordrecht, 2004).
  - [51] G. Y. Guo, H. Ebert, W. M. Temmerman, and P. J. Durham, Phys. Rev. B **50**, 3861 (1994).
  - [52] E. Arola, M. Horne, P. Strange, H. Winter, Z. Szotek, and W. M. Temmerman, Phys. Rev. B **70**, 235127 (2004).
  - [53] V. V. Nemoshkalenko, A. E. Krasovskii, V. N. Antonov, V. N. Antonov, U. Fleck, H. Wonn, and P. Ziesche, Phys. status solidi B **120**, 283 (1983).
  - [54] E. Arola, P. Strange, and B. L. Gyorffy, Phys. Rev. B **55**, 472 (1997).
  - [55] V. N. Antonov, D. A. Kukusta, and L. V. Bekenov, Phys. Rev. B **105**, 155144 (2022).
  - [56] H. k. Müller-Buschbaum and C. Lang, Z. Anorg. Allg. Chem. **568**, 29 (1989).
  - [57] J. L. Campbell and T. Parr, At. Data Nucl. Data Tables **77**, 1 (2001).
  - [58] V. N. Antonov, O. Jepsen, A. N. Yaresko, and A. P. Shpak, J. Appl. Phys. **100**, 043711 (2006).
  - [59] V. N. Antonov, B. N. Harmon, A. N. Yaresko, and A. P. Shpak, Phys. Rev. B **75**, 184422 (2007).
  - [60] V. N. Antonov, A. N. Yaresko, and O. Jepsen, Phys. Rev. B **81**, 075209 (2010).
  - [61] O. K. Andersen, Phys. Rev. B **12**, 3060 (1975).
  - [62] J. P. Perdew, K. Burke, and M. Ernzerhof, Phys. Rev. Lett. **77**, 3865 (1996).
  - [63] P. E. Blöchl, O. Jepsen, and O. K. Andersen, Phys. Rev. B **49**, 16223 (1994).
  - [64] A. N. Yaresko, V. N. Antonov, and P. Fulde, Phys. Rev. B **67**, 155103 (2003).
  - [65] P. H. Dederichs, S. Blügel, R. Zeller, and H. Akai, Phys. Rev. Lett. **53**, 2512 (1984).
  - [66] W. E. Pickett, S. C. Erwin, and E. C. Ethridge, Phys. Rev. B **58**, 1201 (1998).
  - [67] V. N. Antonov, D. A. Kukusta, and L. V. Bekenov, Phys. Rev. B **105**, 155145 (2022).
  - [68] V. N. Antonov, D. A. Kukusta, and L. V. Bekenov, Phys. Rev. B **109**, 165120 (2024).
  - [69] G. van der Laan and B. T. Thole, Phys. Rev. Lett. **60**, 1977 (1988).
  - [70] X. Liu, V. M. Katukuri, L. Hozoi, W.-G. Yin, M. P. M. Dean, M. H. Upton, J. Kim, D. Casa, A. Said, T. Gog, et al., Phys. Rev. Lett. **109**, 157401 (2012).
  - [71] A. Krajewska, T. Takayama, R. Dinnebier, A. Yaresko, K. Ishii, M. Isobe, and H. Takagi, Phys. Rev. B **101**, 121101(R) (2020).
  - [72] X. Lu, P. Olalde-Velasco, Y. Huang, V. Bisogni, J. Pellicari, S. Fatale, M. Dantz, J. G. Vale, E. C. Hunter, J. Chang, et al., Phys. Rev. B **97**, 041102(R) (2018).